

6. H. von Löhneysen, A. Rosch, M. Vojta, P. Wölfle, *Rev. Mod. Phys.* **79**, 1015 (2007).
7. P. Aynajian *et al.*, *Proc. Natl. Acad. Sci. U.S.A.* **107**, 10383 (2010).
8. A. R. Schmidt *et al.*, *Nature* **465**, 570 (2010).
9. P. Wölfle, Y. Dubi, A. V. Balatsky, *Phys. Rev. Lett.* **105**, 246401 (2010).
10. S. Nakatsuji, D. Pines, Z. Fisk, *Phys. Rev. Lett.* **92**, 016401 (2004).
11. Y. F. Yang, Z. Fisk, H. O. Lee, J. D. Thompson, D. Pines, *Nature* **454**, 611 (2008).
12. Th. Pruschke, R. Bulla, M. Jarrell, *Phys. Rev. B* **61**, 12799 (2000).
13. S. Burdin, A. Georges, D. R. Grempel, *Phys. Rev. Lett.* **85**, 1048 (2000).
14. S. Nakatsuji *et al.*, *Phys. Rev. Lett.* **89**, 106402 (2002).
15. T. T. Ong, B. A. Jones, *Phys. Rev. Lett.* **103**, 066405 (2009).
16. H. Shishido *et al.*, *Science* **327**, 980 (2010).
17. Materials and methods are available as supporting material on Science Online.
18. P. Wahl *et al.*, *Phys. Rev. Lett.* **98**, 056601 (2007).
19. For the 2D O₂ lattice formed on Ag(110) with a smaller intermolecular distance, the resonance magnitude can even exceed 100% of the zero-bias conductance (Fig. 3E).
20. U. Fano, *Phys. Rev.* **124**, 1866 (1961).
21. M. Plihal, J. W. Gadzuk, *Phys. Rev. B* **63**, 085404 (2001).
22. M. Ternes, A. J. Heinrich, W. D. Schneider, *J. Phys. Condens. Matter* **21**, 053001 (2009).
23. The intrinsic coherence temperature T^* was deconvoluted from the measured Kondo width Γ by subtracting the contributions from the tip temperature (T_{tip}), sample temperature (T_{sample}), and the bias modulation (V_{ac}): $2\Gamma = \sqrt{(3.2k_B T_{tip})^2 + (5.4k_B T_{sample})^2 + (2\sqrt{2}V_{ac})^2 + (2k_B T^*)^2}$.
24. B. C. Stipe, M. A. Rezaei, W. Ho, *Science* **280**, 1732 (1998).
25. N. Knorr, M. A. Schneider, L. Diekhöner, P. Wahl, K. Kern, *Phys. Rev. Lett.* **88**, 096804 (2002).
26. C. Y. Lin, A. H. Castro Neto, B. A. Jones, *Phys. Rev. Lett.* **97**, 156102 (2006).
27. L. Pauling, *The Nature of the Chemical Bond* (Cornell University Press, Ithaca, NY, 1960).
28. P. Schlottmann, P. D. Sacramento, *Adv. Phys.* **42**, 641 (1993).
29. B. Coqblin, M. D. Núñez-Regueiro, A. Theumann, J. R. Iglesias, S. G. Magalhães, *Philos. Mag.* **86**, 2567 (2006).
30. J. J. Parks *et al.*, *Science* **328**, 1370 (2010).

Acknowledgments: Supported by the National Science Foundation under grant DMR-0606520 (W.H.) and the Department of Energy under grant DE-FG02-05ER46237 (R.W.). Y. J. acknowledges support by the 985 Program of Peking University and the National Science Foundation of China. DFT calculations were performed on supercomputers at the National Energy Research Scientific Computing Center. We thank D. L. Mills, J. M. Lawrence, and W. Ji for enlightening discussions. The authors declare no competing financial interests.

Supporting Online Material

www.sciencemag.org/cgi/content/full/333/6040/324/DC1
Materials and Methods

SOM Text

Figs. S1 to S7

Table S1

References

18 March 2011; accepted 24 May 2011

10.1126/science.1205785

Directing Zeolite Structures into Hierarchically Nanoporous Architectures

Kyungsu Na,^{1,2} Changbum Jo,^{1,2} Jeongnam Kim,¹ Kanghee Cho,^{1,2} Jinhwan Jung,^{1,2} Yongbeom Seo,^{1,2} Robert J. Messinger,³ Bradley F. Chmelka,³ Ryong Ryoo^{1,2*}

Crystalline mesoporous molecular sieves have long been sought as solid acid catalysts for organic reactions involving large molecules. We synthesized a series of mesoporous molecular sieves that possess crystalline microporous walls with zeolitelike frameworks, extending the application of zeolites to the mesoporous range of 2 to 50 nanometers. Hexagonally ordered or disordered mesopores are generated by surfactant aggregates, whereas multiple cationic moieties in the surfactant head groups direct the crystallization of microporous aluminosilicate frameworks. The wall thicknesses, framework topologies, and mesopore sizes can be controlled with different surfactants. The molecular sieves are highly active as catalysts for various acid-catalyzed reactions of bulky molecular substrates, compared with conventional zeolites and ordered mesoporous amorphous materials.

Nanoporous materials possessing pores of molecular dimensions can be used to separate or selectively adsorb guest molecules according to size and shape (1–3). Zeolites are the best-known group of these molecular sieves, constituting a family of crystalline microporous aluminosilicate minerals (~200 structures) (1, 4). The pore diameters, shapes, and connectivities are specified according to their framework structures, which typically have pore diameters <2 nm. Zeolites are also acid catalysts, cation-exchange materials, and nanoparticle supports, and they exhibit high thermal, hydrothermal, and mechanical stabilities (4–6). The framework acidity may be tailored by the substitution of different heteroatoms (for instance, aluminum) into the framework. Thus, zeolites have diverse applications and occupy >40% of the entire solid catalysts

currently used in the chemical industry (6). Nevertheless, zeolite applications are limited to small molecules that can diffuse through the narrow microporous frameworks.

The microporosity of zeolites is generated by the incorporation of pore-generating species such as alkyl-ammonium molecules, which compensate negative charges on the crystallizing silicate framework (4, 7). Such “porogens” can be removed (e.g., by thermal calcination), generating a microporous framework. Several porogens can aggregate to generate pores that are larger than those produced by nonaggregating porogens, but thus far resulting crystalline zeolite structures have been limited to pore diameters <2.2 nm (8). In 1992, Kresge *et al.* reported a supramolecular templating mechanism that used surfactant aggregates as porogens to synthesize ordered mesoporous materials [e.g., Mobil Composition of Matter No. 41 (MCM-41)] (9). The discovery of this supramolecular porogenic mechanism extended the application of molecular sieves to the mesoporous range (2 to 50 nm). Initially, these mesoporous molecular sieves (MMSs) attracted attention as large-pore acid catalysts for various reactions involving

bulky molecules (3, 9, 10). However, due to their noncrystalline frameworks, these MMSs exhibited insufficient framework acidities and, consequently, low catalytic activities (3). Tremendous efforts were made in recent years to synthesize ordered MMSs with crystalline frameworks (11–19). However, such ordered MMSs were difficult to obtain, except for the use of three-dimensionally ordered mesoporous carbon as a template (17). A di-quaternary ammonium surfactant was recently tested as a porogen for such MMSs, but the synthesis yielded two-dimensional (2D) MFI zeolite nanosheets (18, 19).

We present a family of MMSs in which the mesopore walls are zeolitelike microporous crystalline aluminosilicate frameworks. The syntheses were performed with a series of gemini-type, polyquaternary ammonium surfactants that could generate micropores and mesopores simultaneously (fig. S1 and table S1) (20). Hexagonal mesostructures were generated by aggregation of the surfactant molecules, whereas the crystallization of microporous frameworks was directed by quaternary ammonium groups within the mesopore walls. One notable member of this dual-porogenic surfactant family has a molecular formula of C₁₈H₃₇-N⁺(CH₃)₂-C₆H₁₂-N⁺(CH₃)₂-C₆H₁₂-N⁺(CH₃)₂-C₁₈H₃₇(Br⁻)₃ (abbreviated as 18-N₃-18) (Fig. 1A). This surfactant has a zeolite-directing head group composed of three quaternary ammoniums connected with -C₆H₁₂- alkyl spacers and two hydrophobic -C₁₈H₃₇ alkyl tails. Hydrothermal synthesis using this surfactant resulted in a hexagonally ordered MMS with 1.7-nm-thick crystalline MFI-like microporous frameworks (Fig. 1 and figs. S2 and S3). The use of surfactants with different head groups, which include higher numbers of quaternary ammonium groups and the presence of phenyl rings, resulted in MMSs with thicker mesopore walls and different zeolitelike frameworks (Table 1 and figs. S4 to S10). Although the extent of mesostructural order decreases as the wall thickness increases, the thickness of the crystalline walls was uniform

¹Center for Functional Nanomaterials, Department of Chemistry, KAIST, Daejeon 305-701, Korea. ²Graduate School of Nanostructure and Technology (WCU), KAIST, Daejeon 305-701, Korea. ³Department of Chemical Engineering, University of California Santa Barbara (UCSB), Santa Barbara, CA 93106-5080, USA.

*To whom correspondence should be addressed. E-mail: rryoo@kaist.ac.kr

and tailorable over a range of 2.3 to 5.1 nm according to the overall length of the geminilike head groups. The mesopores also exhibited a narrow size distribution, where the mean mesopore diameter could be systematically controlled over 3.8 to 21 nm by the addition of micelle swelling agents, such as 1,3,5-trimethylbenzene. The mesopore arrangement is reminiscent of Korea Advanced Institute of Science and Technology No. 1 (KIT-1) material (figs. S4 to S10), though KIT-1 frameworks are noncrystalline (21).

The synthesis procedure is similar to the hydrothermal crystallization of a typical bulk zeolite, except for the use of dual-porogenic surfactants instead of common organic structure-directing species like tetrapropylammonium. Figure 1 shows scanning electron microscopy (SEM), transmission electron microscopy (TEM), and powder x-ray diffraction (XRD) results of the hexagonally ordered, crystalline MMS, which was synthesized with the 18-N₃-18 surfactant (Fig. 1A). SEM images (Fig. 1B and fig. S2) show uniform nano-

crystals in size and morphology. No amorphous aluminosilicas or bulk zeolite crystals were detected throughout the entire sample. TEM images (Fig. 1, C and D, and fig. S3) show hexagonal arrays of mesopores in the MMS nanocrystals and a microporous framework within the mesopore walls. Images taken perpendicularly to the mesopore walls show crystal lattice fringes with a uniform spacing of 1.16 nm (Fig. 1D and top left inset), indicating that the mesopore walls possess a zeolitic crystalline microporous framework. Figure 1E shows three resolved Bragg reflections in the low-angle XRD region and four more reflections in the high-angle region. The low-angle peaks can be indexed to (10), (11), and (30) reflections (diameter $d = 4.51, 2.57,$ and 1.54 nm, respectively), corresponding to a mesoscale lattice with 2D hexagonal symmetry, similar to MCM-41 (9). The XRD resolution is not sufficient to distinguish the (20) reflection from the (30), which may be the result of small crystallite sizes as shown in the SEM images. The present MMSs show no detectable differences in the 2θ values (where θ is the angle between the incident x-ray and the scattering planes) of the low-angle reflections between as-synthesized and calcined samples. This is different from MCM-41, which experiences framework contraction during calcinations due to continued condensation of the amorphous silica framework. This difference is consistent with the fully condensed crystalline frameworks of the MMS materials. In the high-angle XRD region, four reflections at $d = 1.16, 0.59, 0.39,$ and 0.31 nm are observed, suggesting a regular stacking of lattice planes with uniform spacing of 1.16 nm that is in good agreement with the lattice fringes in the TEM image. The presence of the higher-order reflections beyond 1.16 nm indicates that the MMS framework has atomic-scale ordering. Note that determining the microporous framework structure accurately by XRD is challenging because the mesopore walls are composed of only a single layer of zeolitic micropores, which can be less than a single-unit-cell dimension of a bulk zeolite. In addition, the zeolite-like mesopore walls extend over a very narrow diffractive domain in width. Diffractive interferences may also be considerable between adjacent walls that join at a distinct angle. The XRD reflections under these conditions are thus insufficient for the precise determination of the microporous framework structure.

The gemini-type surfactant species are designed to promote the formation of both nanocrystalline as well as liquid-crystal-like mesostructural order of the zeolite frameworks. The dual roles of the gemini-type dual-porogenic surfactants are elucidated by 2D heteronuclear correlation (HETCOR) nuclear magnetic resonance (NMR) spectroscopy (22), which resolves the molecular proximities of the dual-porogenic surfactant to specific framework moieties. The 2D $^{29}\text{Si}\{^1\text{H}\}$ HETCOR NMR spectrum (Fig. 2) reveals the crucial role of the quaternary ammonium groups in directing crystallization of the zeolite frameworks. A separately acquired 1D ^{29}Si cross-polarization (CP)

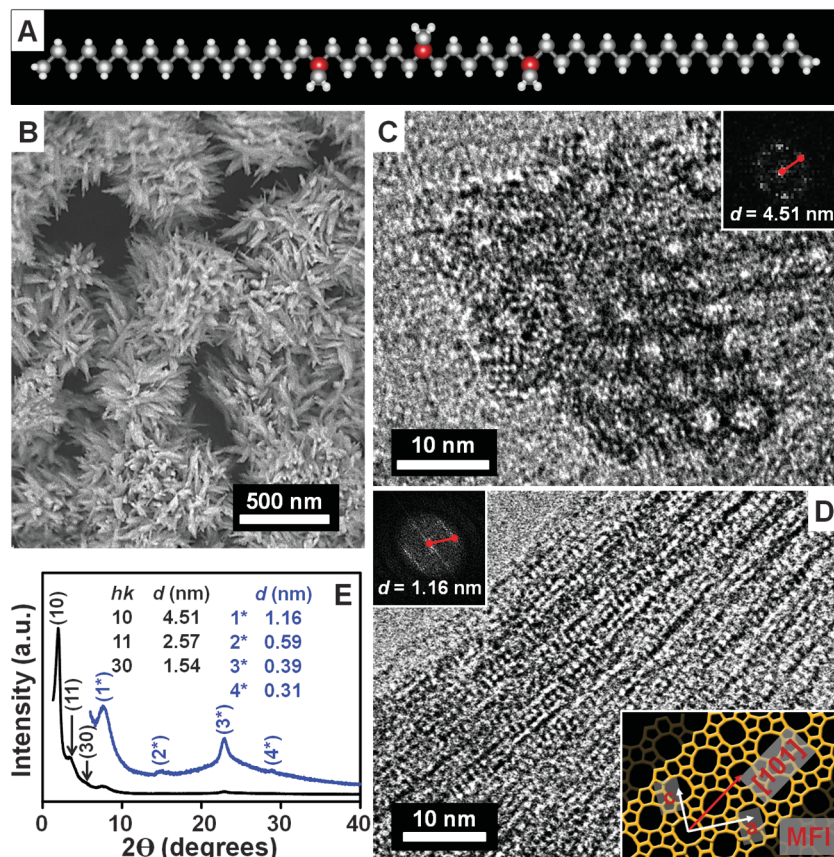


Fig. 1. (A) 18-N₃-18 surfactant (white spheres, hydrogen; gray spheres, carbon; red spheres, nitrogen). (B) SEM, (C and D) TEM, [(C and D), insets] Fourier diffractogram, and (E) XRD pattern of hexagonally ordered crystalline MMS after surfactant removal. For structural comparison, an MFI framework model is given in the bottom right inset of (D) (see also fig. S13). *hk*, Miller indices; a.u., arbitrary units.

Table 1. Structural properties of mesostructured molecular sieves.

| Surfactant* | Zeolite framework | Mesophase | Mean micropore diameter (nm) | Mean mesopore diameter (nm) | BET surface area† (m ² g ⁻¹) | Total pore volume (cm ³ g ⁻¹) | Mesopore wall thickness‡ (nm) |
|------------------------|-------------------|------------|------------------------------|-----------------------------|---|--|-------------------------------|
| 18-N ₃ -18 | MFI-like | Hexagonal | 0.55 | 3.5 | 1190 | 1.58 | 1.7 |
| 22-N ₄ -22 | | | 3.8 | 1060 | 1.48 | 2.3 | |
| N ₄ -phe | Beta | Disordered | 0.65 | 3.6 | 940 | 1.24 | 2.9 |
| N ₆ -diphe | | | 4.5 | 870 | 1.14 | 3.9 | |
| N ₈ -triphe | | | 4.7 | 780 | 0.98 | 5.1 | |

*Gemini-type, poly-quaternary ammonium surfactants used in this work (see table S1 and fig. S1 for chemical formulas and structures). †BET surface area calculated from the adsorption data obtained at P/P_0 between 0.1 and 0.3, using the Brunauer-Emmett-Teller (BET) equation. ‡Mesopore wall thicknesses of crystalline MMSs were determined from the pore diameters of its carbon replicas, except the hexagonally ordered crystalline MMS; its mesopore wall thickness was determined from the BJH mesopore diameter and the hexagonal lattice parameter measured by XRD.

magic-angle-spinning (MAS) spectrum (horizontal axis) exhibits broad signals associated with Q^n ^{29}Si aluminosilicate framework species (23) with increasing extents of condensation. A single-pulse ^1H MAS spectrum (vertical axis) reveals partially resolved ^1H signals from the surfactant molecules whose proton chemical-shift assignments were determined from a 2D $^{13}\text{C}\{^1\text{H}\}$ HETCOR NMR spectrum (fig. S11). The strongest 2D correlated signal intensities associated with Q^3 , $Q^4(1\text{Al})$, and Q^4 ^{29}Si framework species at -100 , -104 , and -109 parts per million (ppm) and $-\text{N}^+\text{CH}_3$ (1 and 6, see Fig. 2) and $-\text{N}^+\text{CH}_2-$ (2 and 5) ^1H moieties at 3.2 ppm provide strong evidence for intermolecular interactions between the ammonium groups and the aluminosilicate frameworks (24). Furthermore, 2D correlated signal intensities between the same ^{29}Si framework species and ^1H signals at 1.6 ppm associated with $-\text{C}_6\text{H}_{12}-$ bridges between alkyl ammonium groups (3 and 4) establish their inclusion within the microporous framework. Importantly, there is an absence of 2D correlated signal intensity between ^{29}Si framework moieties and ^1H signals at 1.3 ppm associated with $-\text{C}_{18}\text{H}_{37}$ alkyl tails (7 and 8), indicating that these tails are mobile and not molecularly proximate to the framework. This observation is consistent with the mesostructure-directing roles of the long hydrophobic surfactant tails. Thus, the quaternary ammonium groups and the $-\text{C}_6\text{H}_{12}-$ alkyl linkages between them interact strongly with the aluminosilicate frameworks, establishing both their role as the zeolite-directing part of the surfactant and their inclusion within the micropores.

The hierarchical porosities of the MMS are evident in their adsorption properties. An argon adsorption isotherm (fig. S12A) of the hexagonal MMS shows three well-resolved increasing steps. The abrupt increase observed in the region of $0.0 < P/P_0 < 0.1$ (where P is the actual adsorption pressure and P_0 is the equilibrium vapor pressure of argon) is a result of micropore filling. The second sharp increase within the $0.4 < P/P_0 < 0.6$ region indicates capillary condensation of Ar in mesopores. The sharp increase above $P/P_0 = 0.8$ is due to Ar condensation in the void volume between particles. The adsorption branch of the capillary condensation region has been used to analyze the mesopore size distribution according to the Barrett-Joyner-Halenda (BJH) algorithm (25). The result shows a very narrow distribution of mesopore diameters centered at 3.5 nm (fig. S12B), similar to MCM-41. The actual pore diameter will be somewhat larger than 3.5 nm because the BJH method tends to underestimate mesopore diameters by ~ 1 nm (26). By subtracting the pore diameter from the hexagonal lattice parameter measured by XRD, the thickness of the mesopore walls is estimated to be less than 1.7 nm. The micropore size distribution within the mesopore walls has been analyzed with nonlocal density functional theory (NLDFT), using the adsorption region below

Fig. 2. Solid-state 2D $^{29}\text{Si}\{^1\text{H}\}$ HETCOR NMR spectrum of the hexagonal MMS ($\text{Si}/\text{Al} = 15$). 1D ^{29}Si CP MAS and single-pulse ^1H MAS spectra are shown along the horizontal and vertical axes, respectively. A schematic diagram of the surfactant molecule is labeled with ^1H signal assignments of covalently bonded protons. Contours are presented to 10% of full signal intensity.

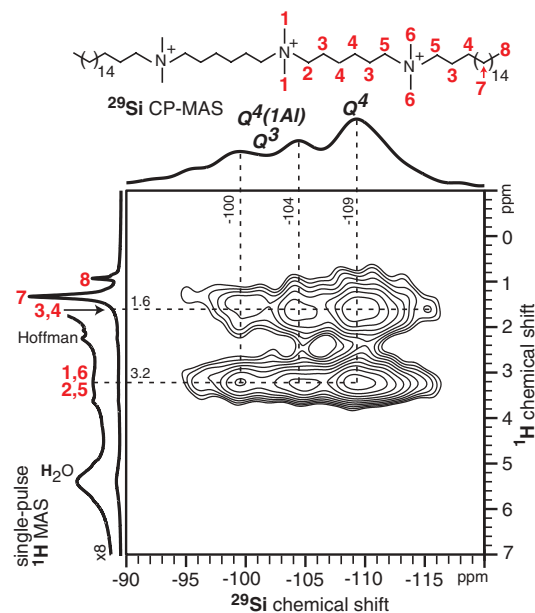
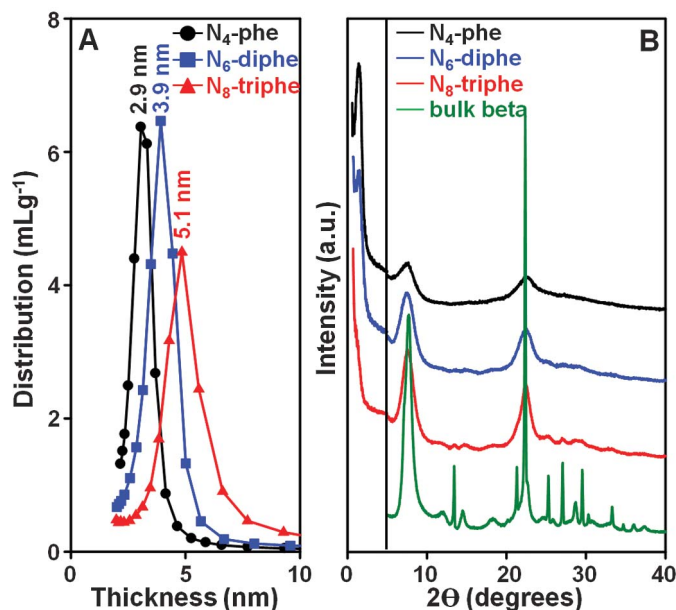


Fig. 3. (A) Framework thickness distributions and (B) XRD patterns of disordered crystalline MMSs synthesized with N_4 -phe (black), N_6 -diphe (blue), and N_8 -triphe (red) surfactants. For comparison, the XRD pattern of bulk beta zeolite is provided (green).

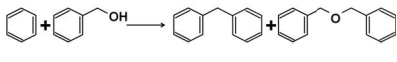
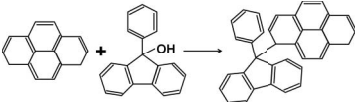
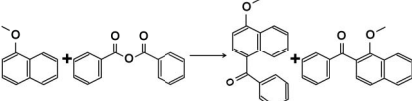
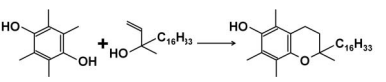


$P/P_0 = 0.1$ (26), revealing bimodal pore size distributions with maxima at 0.55 and 1.2 nm (fig. S12C). The 0.55-nm maximum is higher than that at 1.2 nm, in terms of the corresponding pore volume. The mean pore sizes and pore volume ratios are similar to results obtained by NLDFT analyses of MFI framework. For MFI, the 0.55-nm maximum is attributed to micropores associated with 10-membered oxygen rings (10-MR). The 1.2-nm peak is attributed to a transition in the adsorbate packing density (27) or an orthorhombic-monoclinic transition in the crystal symmetry caused by the gas adsorption (28), which is known to be unique for MFI-type zeolites. Moreover, lattice fringes of the microporous frameworks in the TEM image (Fig. 1C) are similar to those obtained for the MFI topology

(fig. S13). Thus, the microporous aluminosilicate framework of this MMS may be the same as or similar to MFI zeolite.

A notable feature of the dual-porogenic surfactant-driven synthesis route is that the thickness of the crystalline microporous walls can be uniformly tailored by the length of the microporogenic part of the surfactant. For example, the wall thickness can be increased according to the number of ammonium groups. A series of crystalline MMSs has been synthesized with the dual-porogenic surfactants listed in Table 1. The thicknesses of the mesopore walls were determined from the pore diameters of their carbon replicas (29), which exhibited narrow pore-size distributions (Fig. 3A and fig. S14) that indicate uniform mesopore wall thicknesses. The wall

Table 2. Comparison of catalytic conversions over different porous aluminosilicates*.

| Reactions | Hexagonal MMS† (Si/Al = 15) | N ₆ -diphe beta ‡ (Si/Al = 14) | Bulk beta (Si/Al = 15) | Al-MCM-41 (Si/Al = 17) |
|---|-----------------------------|---|------------------------|------------------------|
|  | 44% (71%)§ | 33% (68%)§ | 19% (56%)§ | 8% (86%)§ |
|  | 82% | 59% | <5% | <5% |
|  | 52% (>95%) | 65% (>95%) | <5% (>95%) | <5% (>95%) |
|  | 72% (68%)¶ | 61% (93%)¶ | 20% (26%)¶ | <5% (95%)¶ |

*Catalytic activities are compared on the basis of the same weight of catalyst (see the supporting online material for detailed reaction conditions and procedures). †Hexagonally ordered crystalline MMS synthesized by using the 18-N₃-18 surfactant. ‡Crystalline MMS built with zeolite beta framework synthesized by using N₆-diphe surfactant. §Numbers in parentheses indicate percentage selectivity for diphenylmethane. ||Numbers in parentheses indicate percentage selectivity for 4-benzoyl-1-methoxynaphthalene. ¶Numbers in parentheses indicate percentage selectivity for vitamin E (α -tocopherol).

thicknesses increased from 2.9 to 5.1 nm as the number of quaternary ammonium groups bridged by $-\text{CH}_2\text{C}_6\text{H}_4\text{CH}_2-$ increased from four to eight. The zeolite wall thickness obtained by the carbon replication method may contain systematic errors, due to carbon shrinkage by $\sim 10\%$ and underestimation of pore diameters in the BJH analysis. These errors occur with opposite signs, so that the total error can be less than 10%. Nonetheless, it is noteworthy that the framework thickness of crystalline MMSs can be very finely and systematically tuned as a function of microporogenic group length. A single broad reflection is present in the low-angle XRD patterns (Fig. 3B), indicating modest mesostructural order and consistent with TEM images that show a mesostructured framework with 3D connectivity, similar to KIT-1 (figs. S4 to S10) (21). High-angle XRD reflections become better resolved as their wall thicknesses increase (Fig. 3B) and exhibit reflections that are consistent with those for zeolite beta. Moreover, lattice fringes corresponding to beta zeolite were observed inside the mesopore walls (figs. S7 to S9). The micropores were stacked into two different orientations as in bulk beta zeolite, which has two polymorphs, A and B (30, 31). In addition, the NLDFT analysis confirmed that the micropore diameters of the disordered MMSs were identical to that of beta zeolite having 12-MR micropores (0.65 nm) (fig. S15). Hence, it is reasonable that the bulky $-\text{CH}_2\text{C}_6\text{H}_4\text{CH}_2-$ bridges between ammonium groups were suitable to direct 12-MR micropores. This is comparable to the 10-MR pores generation generated by the $-\text{C}_6\text{H}_{12}-$ bridged 18-N₃-18 surfactant for the

synthesis of the hexagonally ordered MMS. When an MMS was synthesized with the 22-N₄-22 surfactant, the NLDFT analysis also yielded 10-MR micropores of 0.55 nm (fig. S16), but the material has thicker crystalline walls.

The crystalline MMSs are promising as acid catalysts for various organic reactions involving bulky molecules (Table 2), establishing that their catalytic activity is much higher than both bulk beta zeolite and Al-MCM-41 (20). This can be attributed to the facile diffusion through the MMS mesopores, strong acidities of their crystalline zeolitic frameworks, and high concentrations of surface acid sites that are accessible to organic substrates. The acid concentrations were measured quantitatively by titrating the MMS with triphenylphosphine oxide (TPPO) and analyzing the populations and strengths of these sites by ³¹P MAS NMR (fig. S17) (32, 33). Note that TPPO is too large to penetrate into the 12-MR micropores and hence binds exclusively to external acid sites on the mesopore surfaces. According to earlier investigations (32), the ³¹P NMR chemical shift of TPPO increases with increasing binding affinity to Brønsted acid sites. The ³¹P chemical-shift difference is attributed to the strong adsorption of TPPO on protonated Brønsted acid sites on the mesopore walls. The crystalline MMSs titrated with TPPO yield ³¹P NMR signals up to 55.7 ppm compared with 44.3 ppm for Al-MCM-41, which indicates that the crystalline MMSs possess stronger acid sites than Al-MCM-41. Bulk zeolite beta can also yield NMR signals up to 55.7 ppm, but the quantity of the strongest external acid sites is much

smaller than that of crystalline MMSs. Thus, the present MMSs possess high concentrations of strong and accessible external acid sites, as compared with Al-MCM-41 or bulk beta zeolite (table S2).

In the dual-porogenic surfactant-driven synthesis mechanism, mesopores are generated by surfactant aggregates, whereas crystalline microporous zeolite frameworks are generated by multiple quaternary ammonium groups. The wall thickness and framework topology can be adjusted by using surfactants with different geminlike head groups. The mesopore diameters are tailorable according to the surfactant tail length or by the addition of hydrophobic swelling agents. The mesoporous structure and strong zeolitic framework acidity result in substantially improved catalytic activities for various organic reactions involving bulky molecules compared with conventional zeolites or amorphous MMSs. It is also possible to use crystalline MMSs as a selective adsorbent for separation of proteins according to the molecular sizes. Bulky enzyme species can be immobilized via covalent bonding, van der Waals forces, or electrostatic interactions with the zeolite frameworks. Furthermore, the synthesis of MMSs can be extended to other inorganic compositions, such as aluminophosphates.

References and Notes

- A. Corma, *Chem. Rev.* **97**, 2373 (1997).
- U. Ciesla, F. Schüth, *Microporous Mesoporous Mater.* **27**, 131 (1999).
- M. E. Davis, *Nature* **417**, 813 (2002).
- C. S. Cundy, P. A. Cox, *Chem. Rev.* **103**, 663 (2003).
- R. A. Sheldon, R. S. Downing, *Appl. Catal. A Gen.* **189**, 163 (1999).
- R. Rinaldi, F. Schüth, *Energy Environ. Sci.* **2**, 610 (2009).
- J. S. Beck et al., *Chem. Mater.* **6**, 1816 (1994).
- J. Sun et al., *Nature* **458**, 1154 (2009).
- C. T. Kresge, M. E. Leonowicz, W. J. Roth, J. C. Vartuli, J. S. Beck, *Nature* **359**, 710 (1992).
- A. Taguchi, F. Schüth, *Microporous Mesoporous Mater.* **77**, 1 (2005).
- J. Pérez-Ramírez, C. H. Christensen, K. Egeblad, C. H. Christensen, J. C. Groen, *Chem. Soc. Rev.* **37**, 2530 (2008).
- A. Larsson, M. Stöcker, R. Schmidt, *Microporous Mesoporous Mater.* **27**, 181 (1999).
- Y. Liu, W. Z. Zhang, T. J. Pinnavaia, *J. Am. Chem. Soc.* **122**, 8791 (2000).
- Z. T. Zhang et al., *J. Am. Chem. Soc.* **123**, 5014 (2001).
- M. Choi et al., *Nat. Mater.* **5**, 718 (2006).
- K. Egeblad, C. H. Christensen, M. Kustova, C. H. Christensen, *Chem. Mater.* **20**, 946 (2008).
- W. Fan et al., *Nat. Mater.* **7**, 984 (2008).
- M. Choi et al., *Nature* **461**, 246 (2009).
- K. Na et al., *J. Am. Chem. Soc.* **132**, 4169 (2010).
- Materials and methods are available as supporting material on Science Online.
- R. Ryoo, J. M. Kim, C. H. Ko, C. H. Shin, *J. Phys. Chem.* **100**, 17718 (1996).
- A. J. Vega, *J. Am. Chem. Soc.* **110**, 1049 (1988).
- Q^m(m Ab)* ²⁹Si species refer to four-coordinate ²⁹Si atoms covalently bonded to four oxygen atoms with *n* next-nearest-neighbor Si or Al atoms (an integer value between 0 and 4) and *m* next-nearest-neighbor Al atoms (an integer between 0 and *n*).
- M. T. Janicke et al., *J. Am. Chem. Soc.* **120**, 6940 (1998).
- E. P. Barrett, L. G. Joyner, P. P. Halenda, *J. Am. Chem. Soc.* **73**, 373 (1951).
- P. I. Ravikovitch, S. C. O. Domhnaill, A. V. Neimark, F. Schueth, K. K. Unger, *Langmuir* **11**, 4765 (1995).

27. A. Saito, H. C. Foley, *Microporous Mater.* **3**, 543 (1995).
28. E. L. Wu, S. L. Lawton, D. H. Olson, A. C. Rohrman Jr., G. T. Kokotailo, *J. Phys. Chem.* **83**, 2777 (1979).
29. R. Ryoo, S. H. Joo, S. Jun, *J. Phys. Chem. B* **103**, 7743 (1999).
30. J. B. Higgins *et al.*, *Zeolites* **8**, 446 (1988).
31. A. Corma *et al.*, *Chem. Mater.* **20**, 3218 (2008).
32. J. H. Lunsford, W. P. Rothwell, W. Shen, *J. Am. Chem. Soc.* **107**, 1540 (1985).
33. Q. Zhao *et al.*, *J. Phys. Chem. B* **106**, 4462 (2002).

Acknowledgments: This work was supported by the National Honor Scientist Program (20100029665) and World Class University Program (R31-2010-000-10071-0) of the Ministry of Education, Science and Technology in Korea. The work at UCSB was supported by the U.S. NSF under grant CHE-0924654 and the U.S. Department of Energy through the Institute of Multiscale Materials Studies at Los Alamos National Laboratory and Basic

Energy Sciences grant DE-FG02-03ER15467. R.J.M. is grateful to the Warren and Katharine Schlinger Foundation for a doctoral research fellowship. Solid-state NMR measurements were conducted using the Central Facilities of the NSF-supported UCSB Material Research Laboratory through grant DMR-05-20415. A patent has been filed by KAIST that claims new materials, preparation method, and catalytic applications thereof [10-2010-0064200, Korea, and PCT/KR2011/004128, Patent Cooperation Treaty (PCT)]. Author contributions: R.R. planned and supervised the project; K.N. and R.R. wrote the manuscript; K.N., C.J., J.K., and J.J. synthesized surfactants and porous materials and performed XRD, SEM, and adsorption; K.N. performed catalytic investigations; K.C. performed TEM investigations; Y.S. analyzed acidity with ^{31}P NMR; and R.J.M. and B.F.C. performed 2D NMR investigations. B.F.C. (bradc@engineering.ucsb.edu) was responsible for the 2D NMR part. The authors declare that there

are no competing financial interests. R.R., K.N., C.J., J.K., and J.J. are applicants for a patent related to this work. The patent deals with an invention of new materials and their synthesis method and applications. The patent was submitted to Korea on 5 July 2010 with application no. 10-2010-0064200 and submitted to PCT on 7 June 2011 with application no. PCT/KR2011/004128.

Supporting Online Material

www.sciencemag.org/cgi/content/full/333/6040/328/DC1
Materials and Methods

SOM Text

Figs. S1 to S17

Tables S1 and S2

References (34–38)

17 February 2011; accepted 20 May 2011

10.1126/science.1204452

The Unusual Nature of Recent Snowpack Declines in the North American Cordillera

Gregory T. Pederson,^{1,2,3*} Stephen T. Gray,^{3,4} Connie A. Woodhouse,^{3,5} Julio L. Betancourt,⁶ Daniel B. Fagre,¹ Jeremy S. Littell,⁷ Emma Watson,⁸ Brian H. Luckman,⁸ Lisa J. Graumlich⁹

In western North America, snowpack has declined in recent decades, and further losses are projected through the 21st century. Here, we evaluate the uniqueness of recent declines using snowpack reconstructions from 66 tree-ring chronologies in key runoff-generating areas of the Colorado, Columbia, and Missouri River drainages. Over the past millennium, late 20th century snowpack reductions are almost unprecedented in magnitude across the northern Rocky Mountains and in their north-south synchrony across the cordillera. Both the snowpack declines and their synchrony result from unparalleled springtime warming that is due to positive reinforcement of the anthropogenic warming by decadal variability. The increasing role of warming on large-scale snowpack variability and trends foreshadows fundamental impacts on streamflow and water supplies across the western United States.

In the mountains of western North America, snowpack controls the amount of runoff (1, 2), affects temperature through surface albedo feedbacks (3, 4), and influences myriad ecosystem processes (5–8). In much of this region, snowpack declined since the 1950s (2, 9–11), and continued reductions are expected throughout the 21st century and beyond (2, 12). When coupled with increasing demand, additional warming-induced snowpack declines would threaten many

current water storage and allocation strategies (13) and lead to substantial strain on related infrastructure and overall supplies. Climate model simulations shed light on the relationships between greenhouse gas forcing and observed shifts in regional temperatures and hydrology (2), but longer-duration records are needed to characterize the range of natural snowpack variability, particularly at decadal-to-multidecadal time scales (14). Did declines similar in duration, magnitude, and extent occur over the past ~1000 years, or are the recent snowpack losses unprecedented? How were previous snowpack declines driven by known mechanisms of temperature and precipitation variability, and to what degree can decadal-to-multidecadal climate variability amplify or dampen future warming-induced trends?

To address these questions, we developed annually resolved, multi-century to millennial-length (500- to >1000-year) snowpack reconstructions for the headwaters of the Columbia, Missouri, and Colorado Rivers. Collectively, these basins serve as the primary water source for >70 million people, and 60 to 80% of their water originates as snowpack (1, 2). Reconstruc-

tions are based on an extensive network of tree-ring sites and provide information on patterns and processes across spatial and temporal scales relevant to water- and natural-resource management (Fig. 1).

Tree rings have long been used to reconstruct precipitation, drought (15, 16), streamflow (17, 18), and temperature (19, 20), but to date there has been no systematic effort to produce multi-scale snowpack reconstructions for all three of these river basins. Previous studies in the region show that in certain topographic, edaphic, and climatic settings, the amount of water available to trees during the growing season is largely controlled by the amount of water in the antecedent snowpack (18, 21). We capitalized on these snow-water-growth linkages by using existing tree-ring collections from areas where precipitation is dominated by snowfall and by sampling trees known to be sensitive to snowpack (18, 21). To further isolate the snowpack signal, particularly in the northern portions of the study area, we used recently collected tree-ring records from species whose seasonal biology (timing of tree-ring growth) ties them closely to snow (22, 23).

For calibration of the tree-ring-based reconstructions, continuous annual, sub-watershed (roughly 40,000 ± σ 25,000 km²) snowpack data sets were constructed by standardizing individual 1 April snow water equivalent (SWE) records to unit deviation then averaging across all records from each watershed (fig. S1 and table S1) (24). Snowpack as measured on 1 April is a crucial component of regional runoff forecasting and water supply evaluations, and records of 1 April SWE are generally longer than for any other time of the year. In addition, 1 April measurements often approximate maximum SWE accumulation in our study watersheds (4, 11), although peak accumulation timing can vary substantially at individual measurement sites. Elevations of individual measurement sites in the Upper Colorado subregion (Fig. 1) tend to be higher than those in the Greater Yellowstone (2807 ± σ 311 m versus 2307 ± σ 291 m), and sites in the Greater Yellowstone region are higher on average than those in the Northern Rockies (~1550 ± σ 424 m). Overall, the 27 composite snowpack reconstructions

¹U.S. Geological Survey (USGS), Northern Rocky Mountain Science Center, 2327 University Way, Suite 2, Bozeman, MT 59715, USA. ²School of Natural Resources, University of Arizona, 325 Biosciences East, Tucson, AZ 85721, USA. ³Laboratory of Tree-Ring Research, University of Arizona, 105 West Stadium, Tucson, AZ 85721, USA. ⁴Department of Civil and Architectural Engineering, University of Wyoming, Laramie, WY 82071, USA. ⁵School of Geography and Development, 412 Harvill Building, University of Arizona, Tucson, AZ 85721–0076, USA. ⁶USGS, National Research Program, Water Resources Division, Tucson, AZ 85719, USA. ⁷Climate Impacts Group, University of Washington, Post Office Box 355672, Seattle, WA 98195–5672, USA. ⁸Department of Geography, University of Western Ontario, London, Ontario N6A 5C2, Canada. ⁹College of the Environment, University of Washington, Post Office Box 355679, Seattle, WA 98195–5679, USA.

*To whom correspondence should be addressed. E-mail: gpederson@usgs.gov



Supporting Online Material for

Directing Zeolite Structures into Hierarchically Nanoporous Architectures

Kyungsu Na, Changbum Jo, Jeongnam Kim, Kanghee Cho, Jinhwan Jung, Yongbeom Seo, Robert J. Messinger, Bradley F. Chmelka, Ryong Ryoo*

*To whom correspondence should be addressed. E-mail: rryoo@kaist.ac.kr

Published 15 July 2011, *Science* **333**, 328 (2011)
DOI: 10.1126/science.1204452

This PDF file includes:

Materials and Methods
SOM Text
Figs. S1 to S17
Tables S1 and S2
Full Reference List

1. Materials Preparation

1.1 Synthesis of organic surfactants

A series of gemini-type, poly-quaternary ammonium surfactants are synthesized according to the literature procedures (18, 19). The chemical formulas and corresponding abbreviations of these surfactants are summarized in table S1.

For the synthesis of 18-N₃-18 surfactant, C₁₈H₃₇-N⁺(CH₃)₂-C₆H₁₂-Br(Br⁻) and C₁₈H₃₇-N⁺(CH₃)₂-C₆H₁₂-N(CH₃)₂ were prepared separately *via* organic reaction. First, 0.034 mol of N,N'-dimethyloctadecylamine (99%, TCI) and 0.34 mol of 1,6-dibromohexane (99%, TCI) were dissolved in 1000 mL acetonitrile/toluene mixture (1000 wt% per total organic reactants, 1:1 v/v) and heated at 60°C for 12 h. After cooling to room temperature and solvent evaporation, solid product with the formula of C₁₈H₃₇-N⁺(CH₃)₂-C₆H₁₂-Br(Br⁻) was precipitated. This product was further filtered, washed with diethyl ether, and dried in a vacuum oven at 50°C for 2 h. Second, 0.030 mol of 1-bromooctadecane (96%, Acros Organics) and 0.300 mol of N,N,N',N'-tetramethyl-1,6-diaminohexane (99%, TCI) were dissolved in 600 mL acetonitrile/toluene mixture (1:1 v/v) and heated at 60°C for 12 h. After quenching and purification, solid product with the formula of C₁₈H₃₇-N⁺(CH₃)₂-C₆H₁₂-N(CH₃)₂(Br⁻) was obtained. Finally, equimolar amounts of C₁₈H₃₇-N⁺(CH₃)₂-C₆H₁₂-Br(Br⁻) and C₁₈H₃₇-N⁺(CH₃)₂-C₆H₁₂-N(CH₃)₂(Br⁻) were dissolved in acetonitrile (200wt% per total organic reactants) and refluxed for 12 h. After solvent evaporation, the precipitated product was filtered and dried in a vacuum oven at 50°C to obtain the final product, the 18-N₃-18 surfactant. The purity of the final solid product was analyzed by solution-state ¹H NMR, with CDCl₃ as the solvent.

For the synthesis of N₄-phe surfactant, 0.01 mol of 1-bromodocosane (TCI) and 0.1 mol of N,N,N',N'-tetramethyl-1,6-diaminohexane were dissolved in 100 mL acetonitrile/toluene solvent (1:1 v/v) and heated 60°C for 12 h under magnetic stirring. This solution was evaporated for a removal of solvent and then a white solid was precipitated. The solid product with the formula of C₂₂H₄₅-N⁺(CH₃)₂-C₆H₁₂-N(CH₃)₃(Br⁻) as denoted C₂₂₋₆₋₀ was washed using diethyl ether, filtered, and dried in a vacuum oven at 50°C. Subsequently, 0.02 mol of C₂₂₋₆₋₀ and 0.01 mol of α,α'-dichloro-*p*-xylene (TCI) were dissolved in 65 mL chloroform and refluxed for 12 h. This solution was evaporated for a removal of solvent and then a final product (N₄-phe) was precipitated. The solid was washed using diethyl ether, filtered, and dried in a vacuum oven at 50°C.

For the synthesis of N₆-diphe surfactant, 0.01 mol of C₂₂₋₆₋₀ and 0.1 mol of α,α'-dichloro-*p*-xylene were dissolved in 100 mL acetonitrile, which was heated at 60°C for 48 h. After the organic solvent was evaporated, solid product with the formula of C₂₂H₄₅-N⁺(CH₃)₂-C₆H₁₂-N⁺(CH₃)₂-CH₂-(*p*-C₆H₄)-CH₂-Cl(Br⁻)(Cl⁻) as denoted C_{22-6-phe-Cl} was precipitated. This product was washed with diethyl ether, filtered and dried in a vacuum oven at 50°C. Finally, 0.02 mol of C_{22-6-phe-Cl} and 0.01 mol of N,N,N',N'-tetramethyl-1,6-

diaminohexane were dissolved in 100 mL chloroform and refluxed for 24 h. This solution was evaporated for a removal of solvent and then a final product (N₆-diphe) was precipitated. The solid was washed using diethyl ether, filtered, and dried in a vacuum oven at 50°C.

For the synthesis of N₈-triphe surfactant, 0.01 mol of C_{22-6-phe-Cl} and 0.1 mol of N,N,N',N'-tetramethyl-1,6-diaminohexane were dissolved in 100 mL of acetonitrile at 60°C for 24 h. After cooling down to room temperature, the organic solvent was evaporated, then solid product with the formula of C₂₂H₄₅-N⁺(CH₃)₂-C₆H₁₂-N⁺(CH₃)₂-CH₂-(*p*-C₆H₄)-CH₂-N⁺(CH₃)₂-C₆H₁₂-N⁺(CH₃)₃(Br⁻)(Cl⁻)₂ as denoted C_{22-6-phe-6-0} was precipitated. This product was washed with diethyl ether, filtered and dried in a vacuum oven at 50°C. Finally, 0.02 mol of C_{22-6-phe-6-0} and 0.01 mol of N,N,N',N'-tetramethyl-1,6-diaminohexane were dissolved in 100 mL chloroform and refluxed for 24 h. This solution was evaporated for a removal of solvent and then a final product (N₈-triphe) was precipitated. The solid was washed using diethyl ether, filtered, and dried in a vacuum oven at 50°C.

1.2 Synthesis of crystalline mesoporous molecular sieves (MMSs)

A series of crystalline mesoporous molecular sieves (MMSs) were synthesized with the poly-quaternary ammonium surfactants described in table S1, instead of common organic structure-directing species like tetrapropylammonium. In a typical synthesis of hexagonally ordered MMS built with crystalline microporous frameworks, tetraethylorthosilicate (TEOS, 95%, Junsei), NaAlO₂ (42.5wt% Na₂O, 53wt% Al₂O₃, Sigma-Aldrich), NaOH, C₁₈-N₃-C₁₈ surfactant, ethanol and distilled water were mixed to obtain a gel composition of 6.67 Na₂O: 0.75 Al₂O₃: 30 SiO₂: 1.5 C₁₈-N₃-C₁₈ surfactant: 240 ethanol: 2132 H₂O. Water glass (an aqueous solution of sodium silicate, SiO₂/Na = 1.75, 29 wt% SiO₂) may be used as a silica source instead of TEOS. The resultant gel mixture was agitated under magnetic stirring at 60°C for 6 h. The final gel was transferred to a Teflon-coated stainless-steel autoclave, and heated at 140°C for 4 d under tumbling conditions at 60 rpm. After crystallization, the zeolite product was filtered, washed with distilled water and dried at 120°C. The product was calcined at 550°C for 4 h under flowing air in order to remove the organic surfactants.

1.3 Carbon replication of crystalline MMSs

Carbon replication of mesopore channels of the mesoporous channels of the crystalline MMSs was performed according to the literature procedure (29). First, 0.2 g of crystalline MMS (after surfactant removal) was infiltrated with a mixture consisting of sucrose (0.25 g), sulfuric acid (0.015 mL) and distilled water (0.38 g), in a polypropylene bottle. The infiltrated crystalline MMSs were dried at 100°C for 6 h in a drying oven, and which was subsequently increased to 160°C and retained for 6 h. The carbon/crystalline MMS

composite containing partially decomposed sugar after heating was infiltrated again with 65% of the amount of the mixture that was first infiltrated. After heating to 160°C for 6 h again, the black powder was further heated to 450°C for 3 h and subsequently heated to 700°C for 2 h under vacuum using a quartz tube. The crystalline MMS phase in the resultant carbon/crystalline MMS composite was dissolved by successive washing with HF and HCl mixture solution.

2. Characterization

Scanning electron micrograph (SEM) images were taken with a Hitachi S-4800 at a low landing energy (2.0 kV, in gentle-beam mode), without crashing and metal coating. Transmission electron microscope (TEM) images were taken with a JEOL JEM-3010 with an accelerating voltage of 300 kV ($C_s = 0.6$ mm, point resolution 0.17 nm). X-ray diffraction (XRD) patterns were taken with a Rigaku Multiflex diffractometer equipped with Cu K_α radiation (40 kV, 30 mA). Ar adsorption isotherms were measured at liquid argon temperature (87K) with a Micromeritics ASAP2020 volumetric adsorption analyzer. N₂ adsorption isotherms were measured at liquid nitrogen temperature (77K) with a Micromeritics Tristar II volumetric adsorption analyzer. Specific surface areas of materials were calculated from the adsorption data obtained at P/P_0 between 0.1 and 0.3, using the Brunauer-Emmett-Teller (BET) equation. Micropore size distributions were analyzed below $P/P_0 = 0.1$, by applying nonlocal density-functional-theory (NLDFT) (26). Mesopore size distributions were analyzed by using the Barrett-Joyner-Halenda (BJH) algorithm (25).

Solid-state single-pulse ³¹P magic-angle-spinning (MAS) NMR experiments were carried out using a Bruker AVANCE 400 MHz spectrometer with a 9.4 Tesla widebore superconducting magnet operating at a Larmor frequency of 161.923 MHz. A Bruker ¹H/X double-resonance MAS probehead with 4-mm zirconia rotors was used under conditions of MAS at 12.0 kHz. ³¹P MAS NMR spectra were obtained using a pulse length 5 μs, and a recycle delay of 5 s (32, 33). To obtain an adequate signal-to-noise ratio, 1024 and 14000 scans were acquired for the mesoporous and bulk zeolite samples, respectively. Prior to the NMR measurements, triphenylphosphine oxides (TPPO) as a phosphorous probe molecule were adsorbed on the samples, which only bind to external acid sites due to its large size. In a typical adsorption process, 0.1 g of sample was mixed with 0.03 g (for Al-MCM-41) and 0.0125 g of TPPO (for zeolite samples), dissolved in 2 mL of CH₂Cl₂ in the N₂ glove box, and subsequently agitated in an ultrasonic shaker for 1 h. Then, CH₂Cl₂ was removed by applying a vacuum at 70°C for 1 h. Finally, the sample was transferred into the N₂ glove box and then packed into a 4-mm zirconia rotor with a gas-tight Kel-F cap. ³¹P chemical shifts were referenced to phosphoric acid (H₃PO₄).

In order to analyze the relative amount of external acid sites per total number of Al sites,

the total phosphorous and aluminum contents of the samples after ^{31}P NMR measurements were first analyzed by inductively-coupled plasma atomic emission spectroscopy (ICP-AES) (32). The relative quantity of phosphorous chemisorbed on the external acid sites compared to the total amount of phosphorous adsorbed on the samples was analyzed by deconvolution of the quantitative single-pulse ^{31}P NMR spectra. The relative quantity of chemisorbed phosphorous species was multiplied by the total amount of phosphorous obtained from ICP-AES analysis yields the total amount of external acid sites.

Two-dimensional (2D) NMR experiments were performed using a Bruker AVANCE IPSO 500 MHz NMR spectrometer with an 11.74 Tesla widebore superconducting magnet operating at 500.13, 125.69, and 99.35 MHz for ^1H , ^{13}C , and ^{29}Si nuclei, respectively, which are 100%, 1.1%, and 4.7% naturally abundant. A Bruker $^1\text{H}/\text{X}$ double-resonance MAS probehead with 4-mm zirconia rotors was used under conditions of MAS at 12.5 kHz. For ^1H single-pulse experiments, radio frequency (rf) pulse lengths and power levels were optimized to achieve a 90° rotation of the net ^1H magnetization (2.5 μs pulse). All ^{13}C and ^{29}Si NMR spectra were acquired with simultaneous proton decoupling by applying the Small Phase Incremental Alternation using 64 steps (SPINAL-64) pulse sequence with a ^1H rf field of 100 kHz. All $^{13}\text{C}\{^1\text{H}\}$ and $^{29}\text{Si}\{^1\text{H}\}$ cross-polarization measurements were conducted adiabatically using a contact time of 1.0 and 4.0 ms, respectively. The HETCOR NMR technique is a 2D extension of the 1D CP-MAS NMR experiment, providing enhanced spectral resolution. During the 2D HETCOR experiment, ^1H magnetization evolves for an incremented spin evolution time period t_1 prior to transfer of ^1H magnetization to nearby (< 1 nm) ^{13}C or ^{29}Si spins, whose subsequent NMR free-induction decays are measured directly during the acquisition time t_2 . Double Fourier transformation converts the time domain signal $S(t_1, t_2)$ into the frequency domain $S(\omega_1, \omega_2)$, which is presented here as a 2D contour plot spectrum to 10% of full signal intensity. ^1H - ^1H homonuclear decoupling was applied during the proton spin evolution time t_1 with a phase-modulated rf pulse of constant amplitude (100 kHz) using the eDUMBO-1₂₂ (experimental Decoupling Using Mind Boggling Optimization) pulse sequence (33). A magic-angle ^1H pre-pulse of 1.0 μs was applied after t_1 but prior to cross polarization to rotate the net proton magnetization from the effective plane under homonuclear decoupling to the transverse plane in the rotating frame of reference. A scaling factor of $\lambda = 0.625$ was applied in the indirect ^1H dimension, which was separately calibrated using 2D $^1\text{H}\{^1\text{H}\}$ spin diffusion NMR experiments. Hypercomplex time-proportional-phase-incrementation (STATES-TPPI) quadrature detection was used for the indirect dimension. ^1H , ^{13}C , ^{29}Si chemical shifts were referenced to tetramethylsilane (TMS, $\text{Si}(\text{CH}_3)_4$) with tetrakis(trimethylsilyl)silane (TKS, $\text{Si}[\text{Si}(\text{CH}_3)_3]_4$) as a ^1H and ^{29}Si secondary chemical shift reference and adamantane ($\text{C}_{10}\text{H}_{16}$) as a ^{13}C secondary chemical shift reference.

For NH_3 temperature-programmed desorption (TPD) measurement, 50 mg of calcined

powder sample was introduced into a quartz reactor and degassed under vacuum at 550°C. After cooling to room temperature, NH₃ gas was adsorbed for 1 h, which was followed by desorption at 120°C for removing free and weakly physisorbed NH₃. Desorption profile was then measured using a TCD (thermal conductivity detector) with a temperature decrease of 10°C min⁻¹.

3. Catalytic Tests

For catalytic reaction testing, all catalysts were first NH₄⁺-ion exchanged with a 1 M NH₄NO₃ solution three separate times (NH₄NO₃/Al = 10), and then, subsequently converted to the H⁺ form through calcination in air at 550°C. Prior to all catalytic reactions, the samples were degassed under vacuum at 300°C.

3.1 Reagents

All reagents were received from Sigma Aldrich and used without further purification.

3.2 Friedel–Crafts alkylation of benzene with benzyl alcohol

Alkylation reaction was performed using a Pyrex batch reactor (EYELA chemistation) equipped with a reflux condenser. Typically, 17.5 mL of benzene (190 mmol), 0.75 mL of benzyl alcohol (7.24 mmol) and 50 mg catalyst were placed into the Pyrex chemistation reactor and heated under stirring for 5 h at 80°C. After being cooled to room temperature, the solid catalysts were filtered and the remaining liquid was analyzed on a gas chromatograph equipped with a flame ionization detector and a HP–Innowax capillary column (J&W Scientific: a 30-m-long, 0.32-mm-i.d., and 0.25-μm-thick). The conversion was calculated based on benzyl alcohol.

3.3 Friedel–Crafts alkylation of pyrene with 9–phenyl–9–fluorenyl

For the alkylation reaction, 0.1 g of pyrene (0.5 mmol), 0.258 g of 9–phenyl–9–fluorenyl (1.0 mmol), 6 mL of chloroform and 50 mg catalyst were placed into the Teflon-lined stainless-steel autoclave reactor and heated under tumbling for 2 h at 130°C. After cooling to room temperature, the solid catalysts were filtered and the remaining liquid was analyzed with solution-state ¹H NMR with CDCl₃ as a solvent. The conversion was calculated based on pyrene.

3.4 Friedel–Crafts acylation of 1–methoxynaphthalene with benzoic anhydride

For the acylation reaction, 0.145 mL of 1–methoxynaphthalene (1.0 mmol), 0.113 g of benzoic anhydride (0.5 mmol), 6 mL of chloroform and 50 mg catalyst were placed into the Teflon-lined stainless-steel autoclave reactor and heated under tumbling for 8 h at 150°C. After being cooled to room temperature, the solid catalysts were filtered and the liquid part

of reaction mixture was analyzed on a gas chromatograph equipped with a flame ionization detector and a HP-1 capillary column (J&W Scientific: a 30-m-long, 0.32-mm-i.d., and 0.25- μ m-thick). The conversion was calculated based on benzoic anhydride.

3.5 Synthesis of vitamin E (α -tocopherol)

For synthesis of vitamin E, 0.376 g of trimethylhydroquinone (2.48 mmol), 0.575 mL of isophytol (1.65 mmol), 4 mL of propylene carbonate, 2 mL of heptane and 50 mg catalyst were placed into the Pyrex chemistation reactor and heated under stirring for 5 h at 70°C. After being cooled to room temperature, the solid catalysts were filtered and the remaining liquid was analyzed on a gas chromatograph equipped with a flame ionization detector and a HP-1 capillary column. The conversion was calculated based on isophytol.

4. Supporting Text for Catalytic Reactions

Friedel-Crafts alkylation of aromatic compounds has been one of the most important C-C bond-forming processes for the production of valuable aromatic chemicals (34, 35). Friedel-Crafts acylation of aromatic compounds produces aromatic ketones that are intermediates for the production of fine, pharmaceutical, cosmetic, and agro chemicals (36, 37). However, the aromatic substrates and corresponding products are often too bulky to diffuse through micropores of ordinary bulk zeolites. In this work, we tested our mesoporous zeolitic materials as heterogeneous acid catalysts for Friedel-Crafts alkylation reactions of benzene and pyrene, Friedel-Crafts acylation of 1-methoxynaphthalene, and the synthesis of vitamin E. The results summarized in Table 2 indicate that the catalytic activity of the present materials is much higher than both bulk beta zeolite and Al-MCM-41. The high catalytic performance can be explained in terms of facile molecular diffusion into the mesopores (*i.e.*, accessibility of the catalytic sites) and strong acid sites therein. For the benzene alkylation, the substrates and corresponding products can diffuse into the micropore apertures. A significant catalytic activity can be observed even when the solely microporous bulk beta zeolite was used. However, since the hexagonal MMS and N₆-diphe beta zeolites have very thin zeolitic framework with secondary mesoporosity, they exhibit higher catalytic activity than both bulk beta zeolite and Al-MCM-41. On the contrary, when the substrates are much larger (*i.e.*, pyrene), the difference in catalytic conversion becomes much larger due to the diffusion limitations of reactants and products. The very low catalytic conversion over Al-MCM-41 is attributed to the low acid strength as evidenced by ³¹P NMR (fig. S17, table S2).

In addition to the Friedel-Crafts alkylation, Friedel-Crafts acylation of 1-methoxynaphthalene is a diffusion-controlled, acid-catalytic reaction. Since 1-methoxynaphthalene is sterically hindered for diffusion into the zeolite micropores, the catalytic conversion over solely microporous bulk beta zeolite is negligible. In terms of product selectivity, benzoylation of 1-methoxynaphthalene occurs normally at the 2- or 4-position in the naphthalene ring (37). The high product selectivity for 4-benzoyl-1-methoxynaphthalene after 1-methoxynaphthalene acylation reaction is due to the steric constraint of the transition state during the formation of 2-benzoyl-1-methoxynaphthalene.

Similarly, in the vitamin E (α -tocopherol) synthesis reaction, the crystalline MMSs exhibit high catalytic activity and product selectivity as compared to the bulk beta and Al-MCM-41. This reaction is known to be preceded by condensation of hydroxyl group at Brønsted acid sites, and also by alkylation of olefin group at Lewis acid sites. The catalytic results suggest that the crystalline MMSs possess both Brønsted and Lewis acid sites with sufficient amount. In addition, the shorter diffusion pathways compared to the bulk beta zeolite can produce vitamin E with higher selectivity. That is, in the case of bulk beta zeolite, the diffusion pathway through the bulk zeolite crystals can be very long. Thus, vitamin E can be further catalyzed by acid sites, and hence its product selectivity seems to be low compared to the crystalline MMSs.

5. Figures

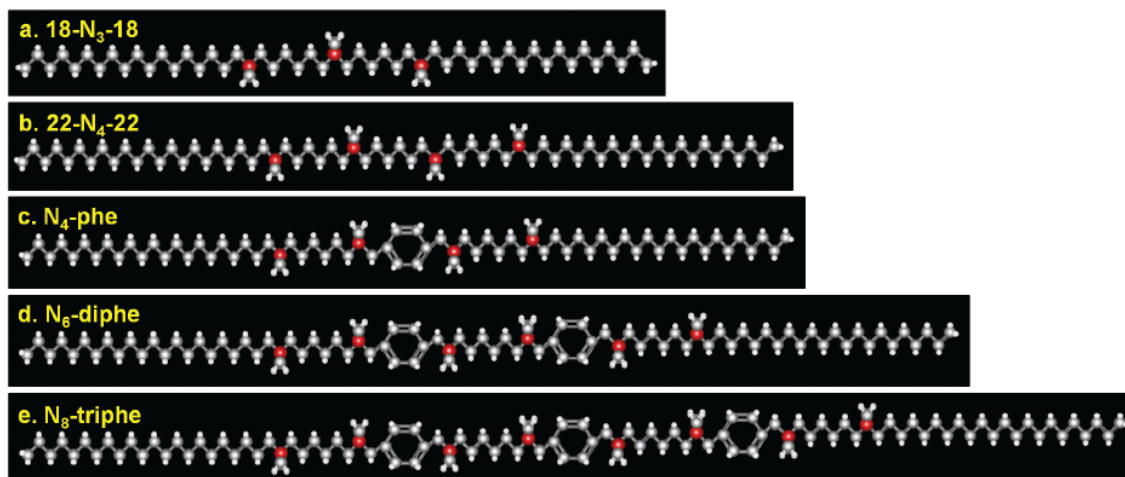


Fig. S1. Gemini-type poly-quaternary ammonium organic surfactants, (a) 18-N₃-18, (b) 22-N₄-22, (c) N₄-phe, (d) N₆-diphe and (e) N₈-triphe from top to bottom, respectively (white spheres, hydrogen; gray spheres, carbon; red spheres, nitrogen). For simplification, counter anions (*i.e.*, Cl⁻ and Br⁻) for quaternary ammoniums are omitted.

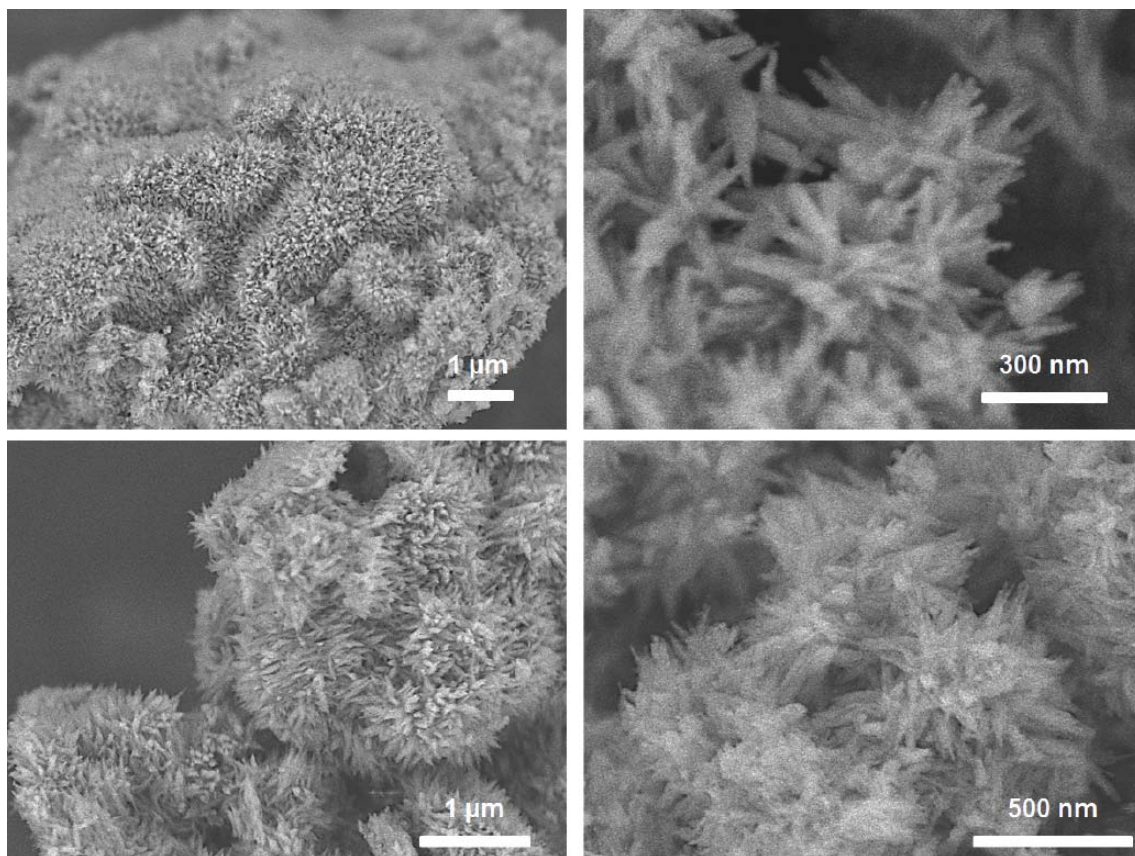


Fig. S2. SEM images of a hexagonally ordered crystalline MMS synthesized with the 18-N₃-18 surfactant.

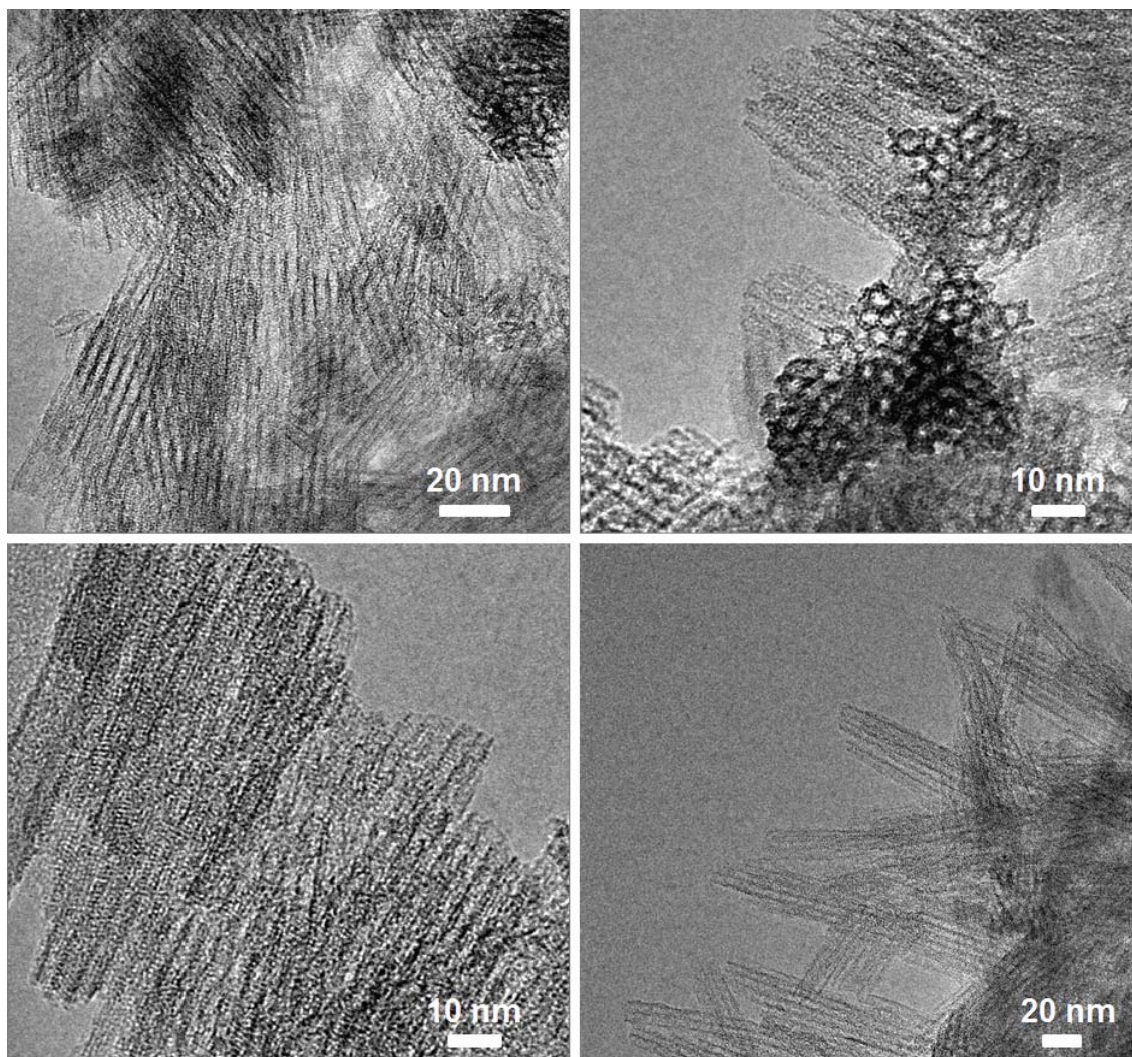


Fig. S3. TEM images of a hexagonally ordered crystalline MMS synthesized with the 18-N₃-18 surfactant.

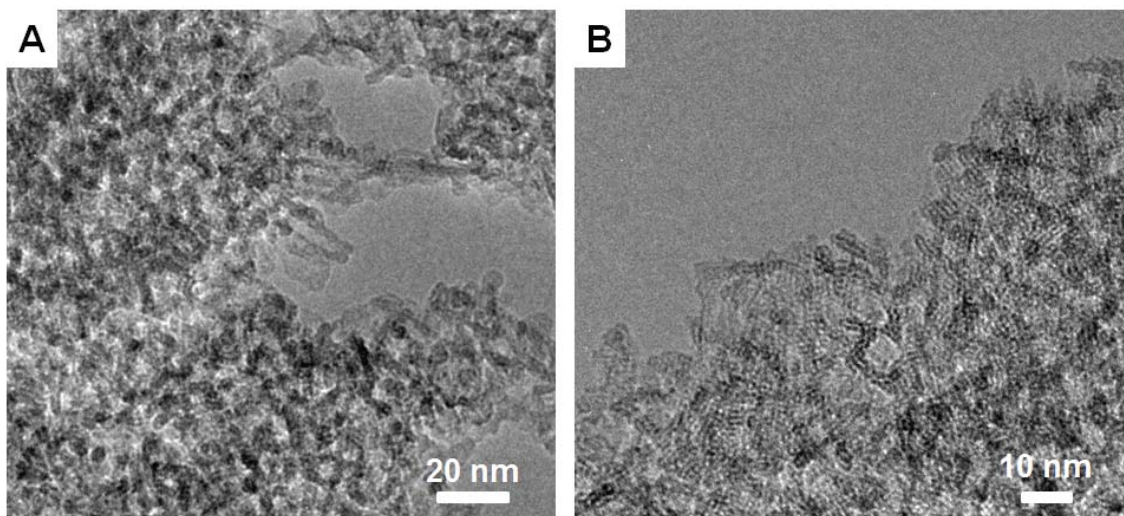


Fig. S4. TEM images of a disordered crystalline MMS synthesized with the 22-N₄-22 surfactant.

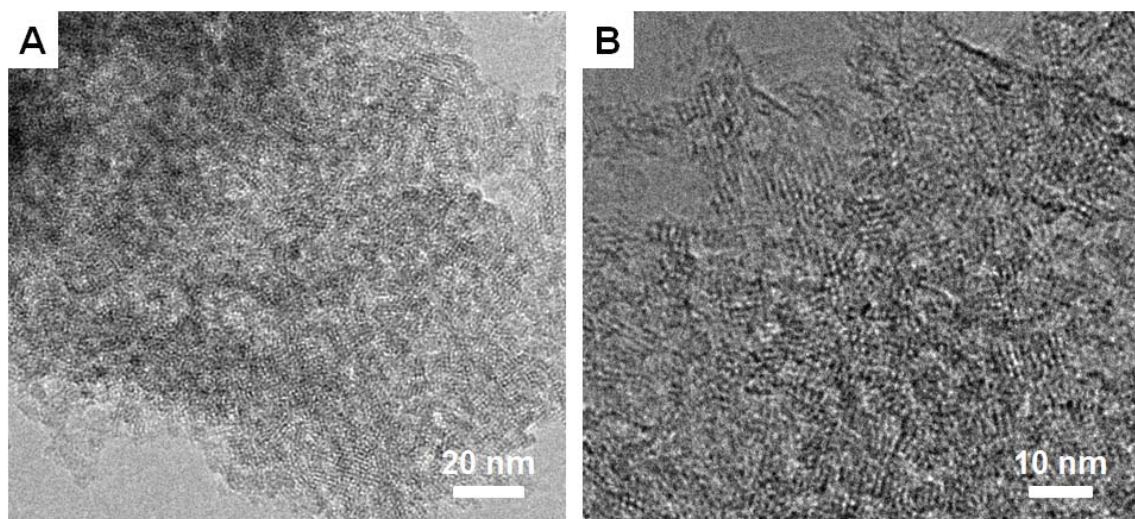


Fig. S5. TEM images of a disordered crystalline MMS built with zeolite beta frameworks synthesized with the N₄-phe surfactant.

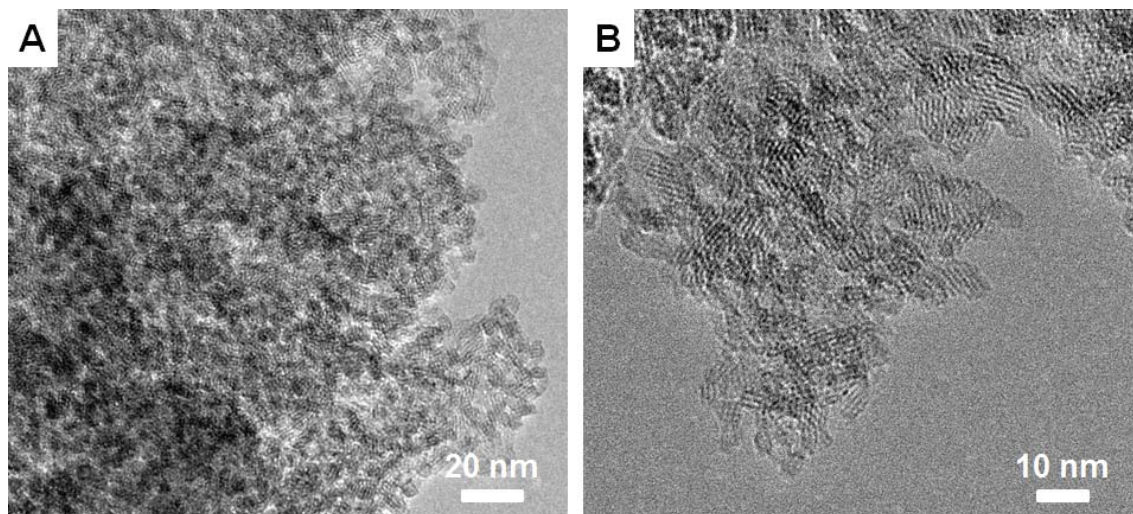


Fig. S6. TEM images of a disordered crystalline MMS built with zeolite beta frameworks synthesized with the N_6 -diphe surfactant.

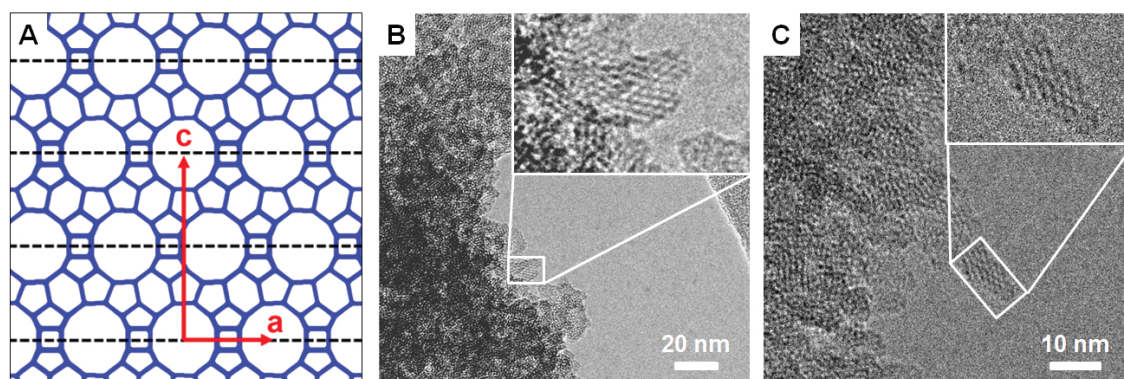


Fig. S7. (A) Schematic diagram of polymorph A in the zeolite beta framework (ref. 31) and (B and C) TEM images of a disordered crystalline MMS built with zeolite beta frameworks synthesized with the N_6 -diphe surfactant. TEM images indicate that the present MMS contains micropore stackings in polymorph A as in zeolite beta framework.

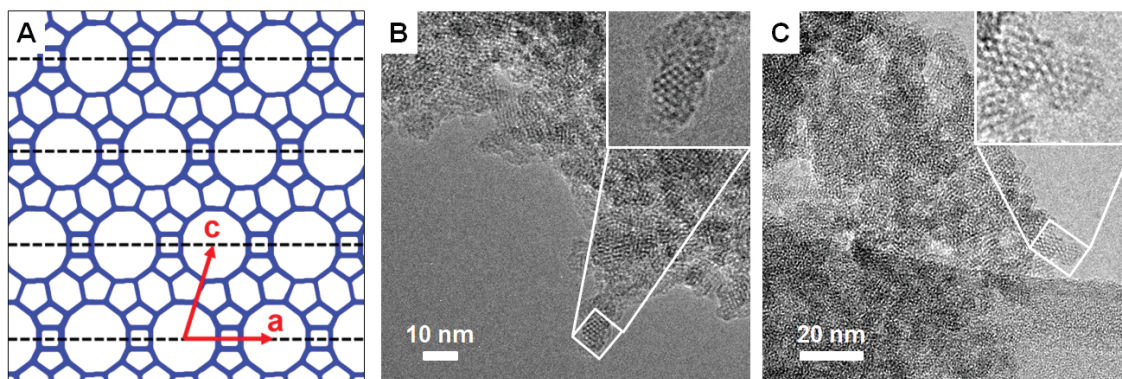


Fig. S8. (A) Schematic diagram of polymorph B in the zeolite beta framework (ref. 31) and (B and C) TEM images of a disordered crystalline MMS built with zeolite beta framework synthesized with the N₆-diphe surfactant. TEM images show that the present MMS contains micropore stackings in polymorph B as in zeolite beta framework.

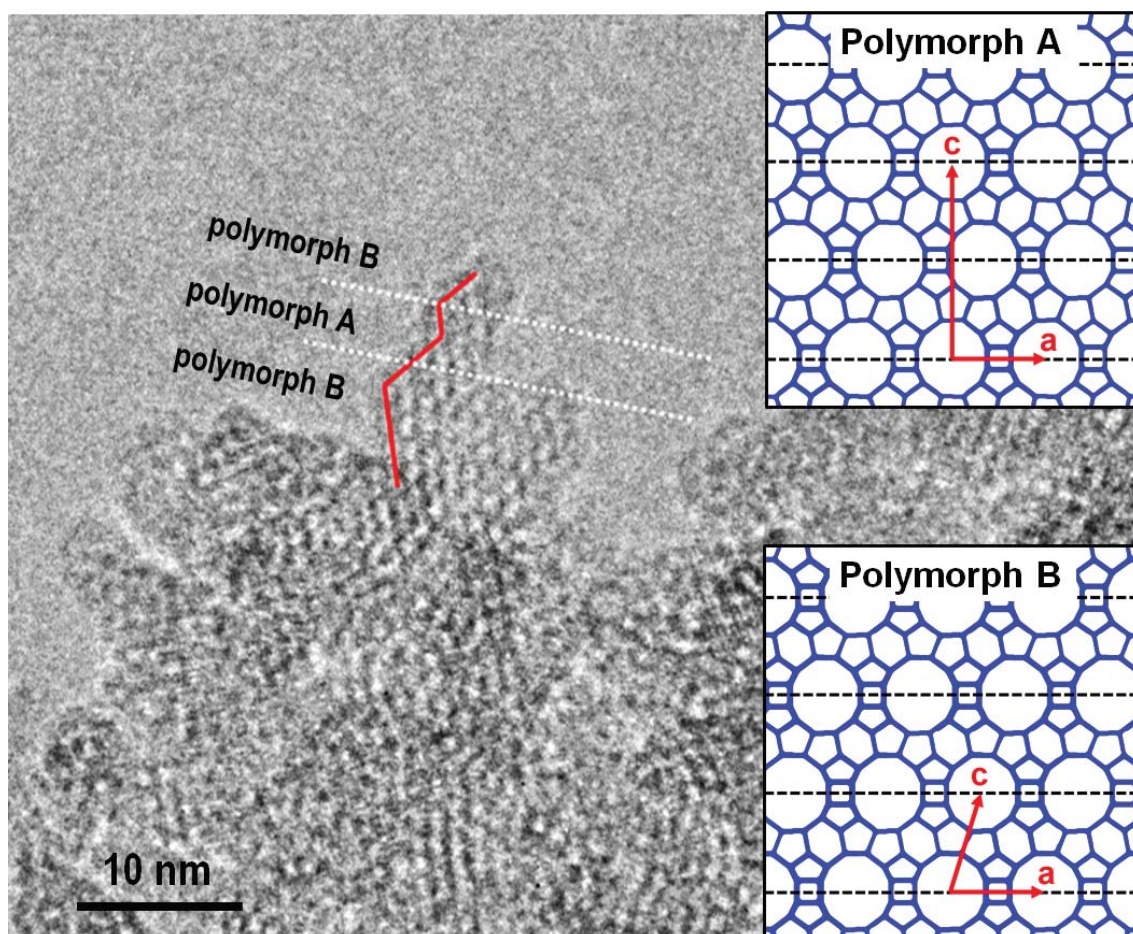


Fig. S9. TEM image of a disordered crystalline MMS built with zeolite beta framework synthesized with the N_6 -diphe surfactant, showing an intergrown crystal of both polymorph A and B.

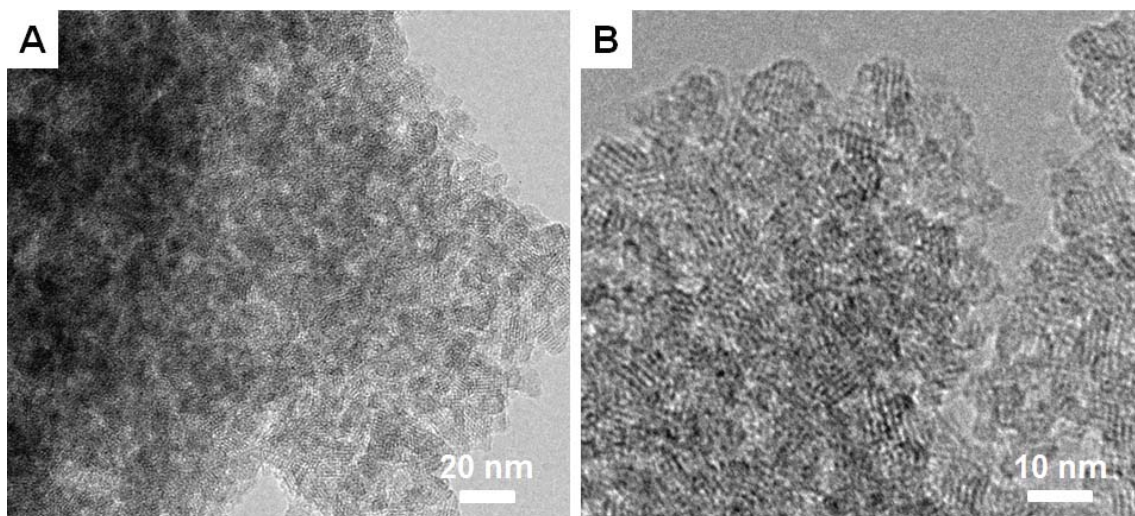


Fig. S10. TEM images of a disordered crystalline MMS built with zeolite beta framework synthesized with the N₈-triphe surfactant.

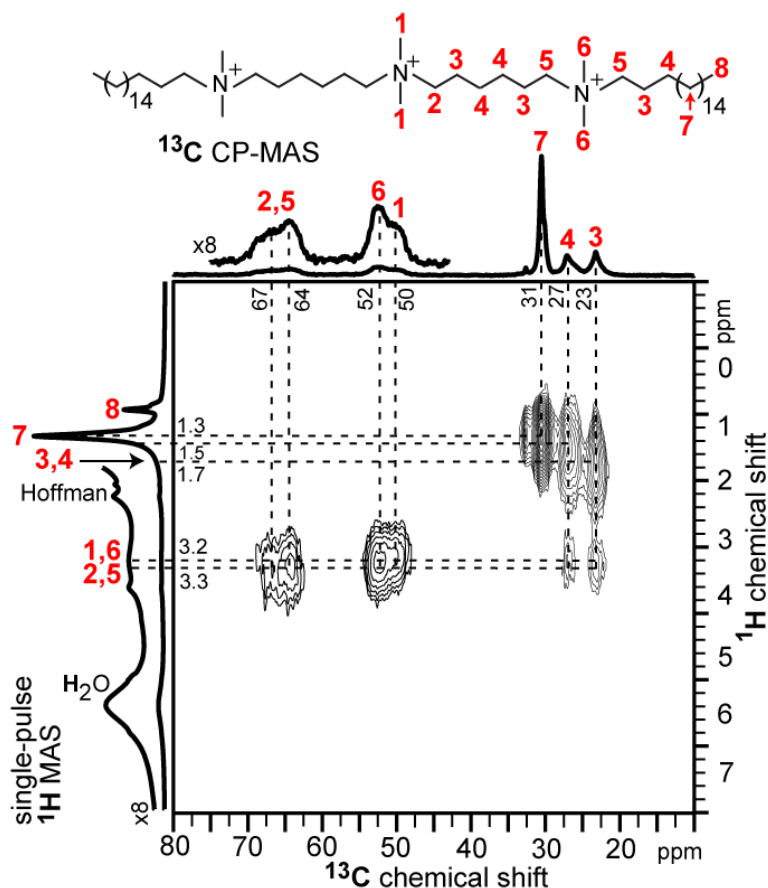


Fig. S11. Solid-state 2D $^{13}\text{C}\{^1\text{H}\}$ HETCOR NMR spectrum of a hexagonally ordered crystalline MMS (Si/Al=15) synthesized with the 18-N₃-18 surfactant. 1D ^{13}C CP-MAS and single-pulse ^1H MAS spectra are shown along the horizontal and vertical axes, respectively. A schematic diagram of the surfactant molecule is labeled with signal assignments for ^{13}C moieties and their covalently bonded protons. All spectra were acquired under conditions of 12.5 kHz MAS at room temperature. A ^{13}C - ^1H CP contact time of 1 ms was used. Contours are presented to 10% of full signal intensity.

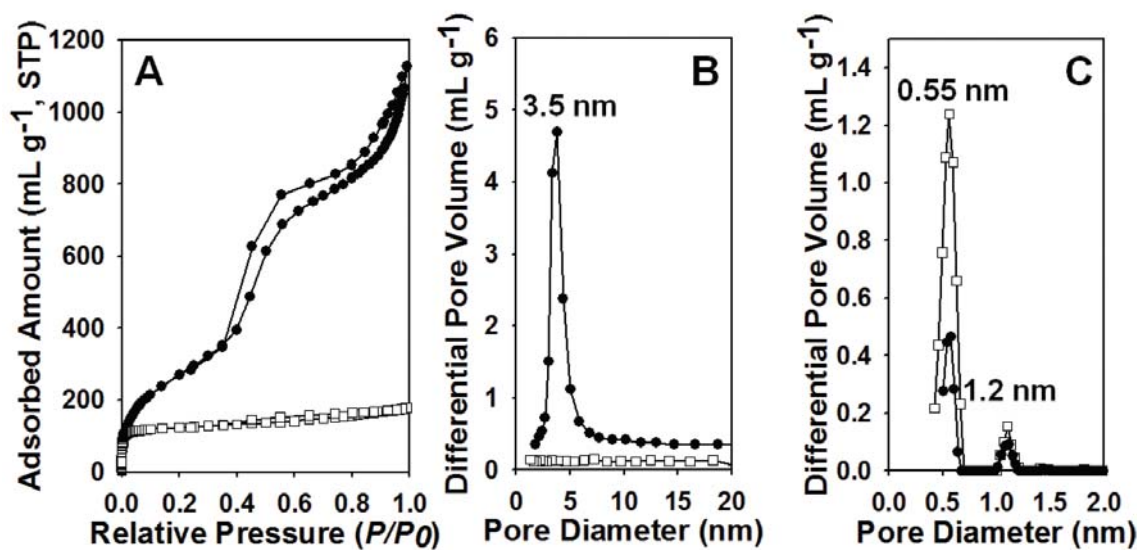


Fig. S12. (A) Ar adsorption isotherm, (B) BJH mesopore size distribution, and (C) NLDFT micropore size distribution of a hexagonally ordered crystalline MMS synthesized with the 18-N₃-18 surfactant, where P is the adsorption pressure and P_0 is the equilibrium vapor pressure of Ar. For comparison, Ar adsorption data of bulk MFI zeolite are also provided (white square plots).

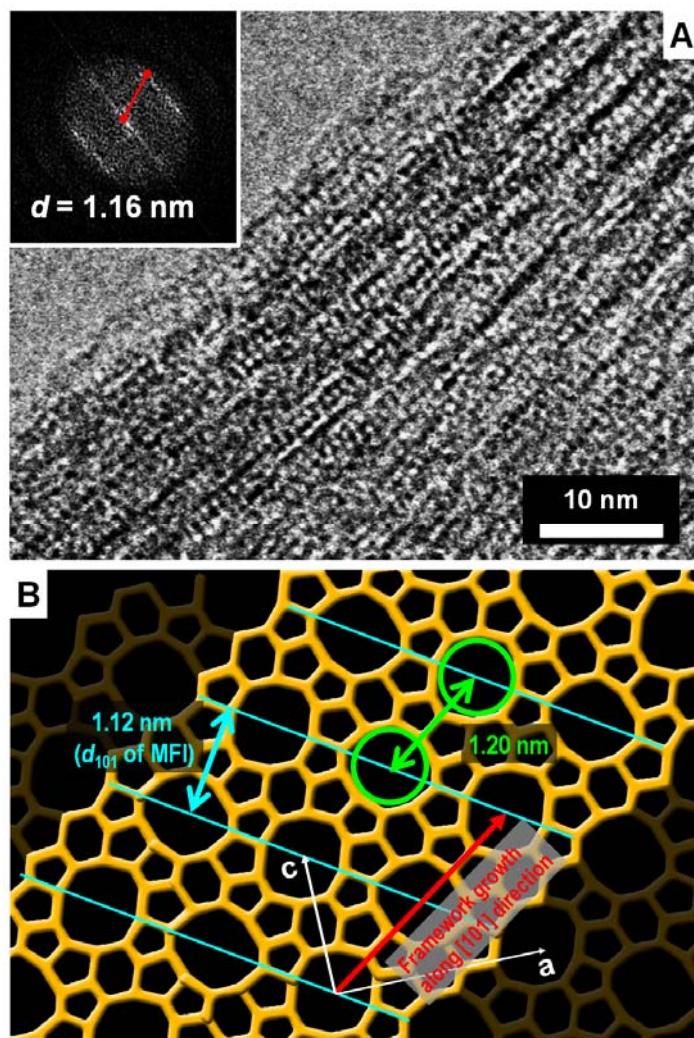


Fig. S13. Proposed framework structure of the hexagonally ordered crystalline MMS. (A) TEM image of a hexagonally ordered crystalline MMS and (B) structural model of the MFI framework (also refer to the reference 38 for lattice fringes of MFI framework). The TEM image corresponds to the side-view of the hexagonal mesopore channels, which shows a regular interplanar spacing of 1.16 nm (refer to an electron diffraction pattern in the inset). The structure of the microporous arrangements might be determined by correlating the electron diffraction patterns with the structural model of the MFI framework (B). The regular arrangement of lattice fringes can be fairly matched to the framework growth along the [101] direction on the (a - c) plane of an MFI framework structure (B). However, no 1.16-nm d -spacings are detected in the XRD pattern of bulk MFI frameworks. This might be attributed to the occurrence of considerable destructive interferences in large bulk crystals. On the contrary, if the zeolite crystals are extremely thin, such destructive diffractions could be dissipated. Hence, the 1.16-nm spacing in TEM might occur from diffractive interferences between 1.12-nm (d_{101}) interplanar spacings and 1.20-nm intermicropore spacings in the MFI framework. More detailed study for the accurate determination of microporous framework structure is challenging.

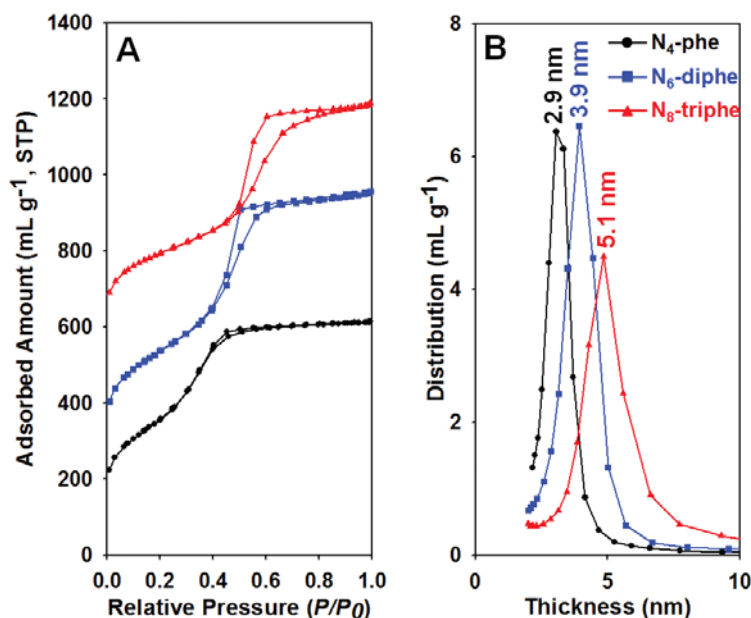


Fig. S14. (A) N₂ adsorption isotherms of carbon replicas of crystalline MMSs synthesized with N₄-phe (black), N₆-triphe (blue) and N₈-triphe (red) surfactants, and (B) corresponding mesopore size distributions calculated by BJH algorithm, where P is the adsorption pressure and P_0 is the equilibrium vapor pressure of N₂.

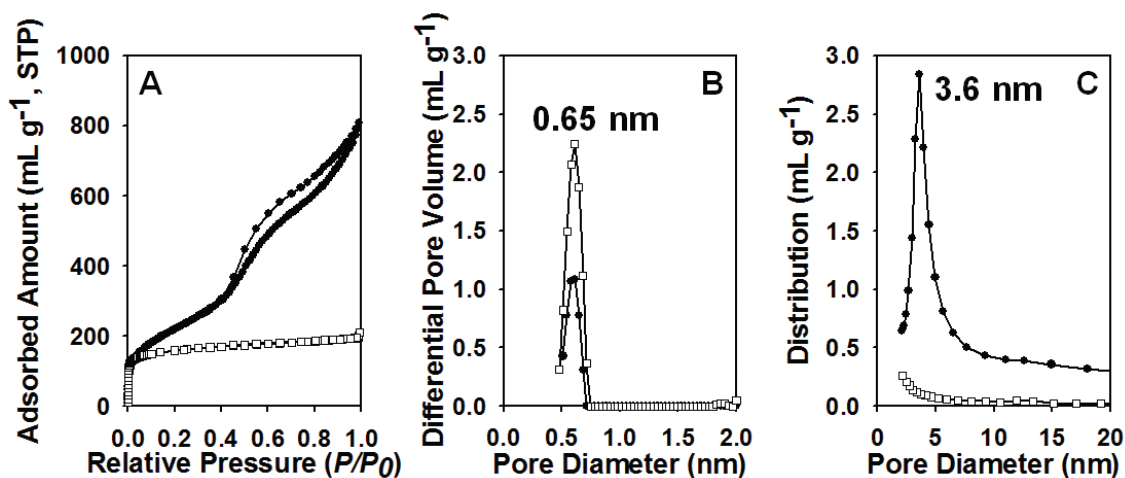


Fig. S15. (A) Ar adsorption isotherm, (B) NLDFT micropore size distribution and (C) BJH mesopore size distribution of a disordered crystalline MMS built with zeolite beta frameworks synthesized with the N₄-phe surfactant, where P is the adsorption pressure and P_0 is the equilibrium vapor pressure of Ar. For comparison, Ar adsorption data of bulk beta zeolite are provided (white square plots)

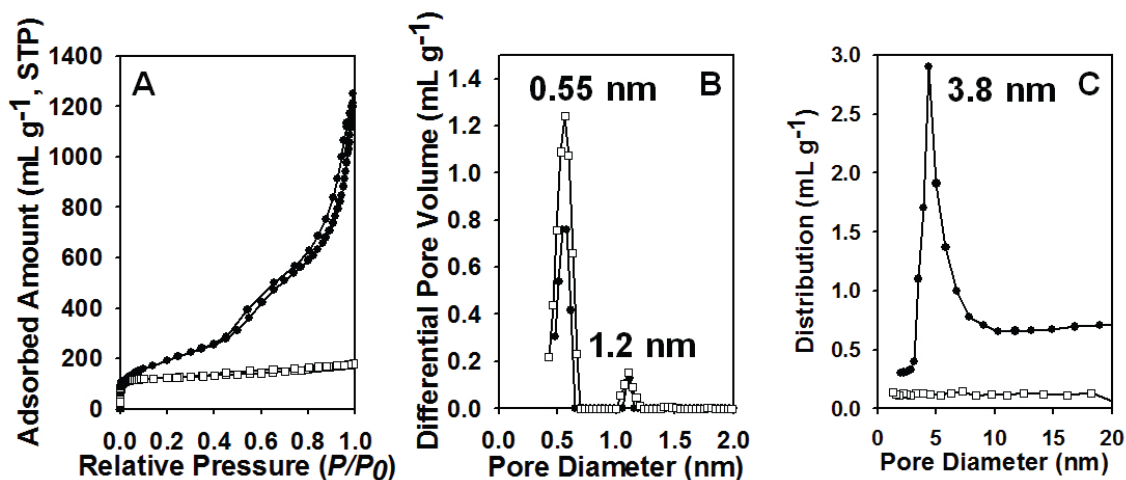


Fig. S16. (A) Ar adsorption isotherm, (B) NLDFT micropore size distribution and (C) BJH mesopore size distribution of a disordered crystalline MMS synthesized with the 22-N₄-22 surfactant, where P is the adsorption pressure and P_0 is the equilibrium vapor pressure of Ar. For comparison, Ar adsorption data of bulk MFI zeolite are provided (white square plots)

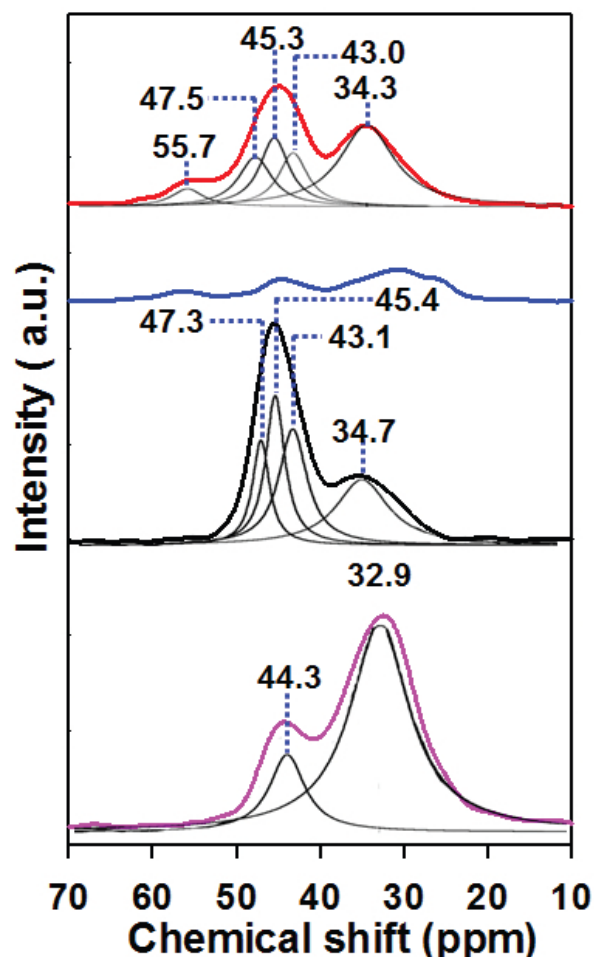


Fig. S17. ^{31}P MAS NMR spectra of triphenylphosphine oxide adsorbed on bulk beta zeolite (Si/Al = 15, blue), Al-MCM-41 (Si/Al = 17, purple) and crystalline MMSs synthesized with the 18-N₃-18 (Si/Al = 15, black) and N₆-diphe (Si/Al = 14, red) surfactants. The ^{31}P NMR chemical shift of TPPO increases with its increasing binding affinity to a Brønsted acid site. Due to the large size of the molecule, TPPO cannot penetrate into the 12-MR micropores. Hence, it can exclusively detect acid sites that are located on the external surface of mesopore walls. The ^{31}P NMR spectra show that the crystalline MMSs yield a ^{31}P NMR signal at the high chemical shift of 55.7 ppm (for the N₆-diphe surfactant-directed material) and 47.3 ppm (for the 18-N₃-18 surfactant-directed material) after the adsorption of TPPO. These NMR signals are attributed to the strong adsorption of the oxygen atom in TPPO on the protonated Brønsted acid sites that exist on the mesopore walls. Thus, the present MMSs have been confirmed to possess strong acid sites at high external concentrations on the mesopore walls, as compared with Al-MCM-41 or bulk zeolite beta. In the case of the bulk zeolite, there are strong acid sites both on the external surface of the crystals and inside micropores. However, the number of strong acid sites available on the external surface is limited by the low external surface area.

6. Tables

Table S1. Chemical formulas of gemini-type, poly-quaternary ammonium organic surfactants used in this work and the corresponding abbreviations.

| Chemical formula | Abbreviation |
|--|------------------------|
| $C_{18}H_{37}-N^+(CH_3)_2-C_6H_{12}-N^+(CH_3)_2-C_6H_{12}-N^+(CH_3)_2-C_{18}H_{37}(Br^-)_3$ | 18-N ₃ -18 |
| $C_{22}H_{45}-N^+(CH_3)_2-C_6H_{12}-N^+(CH_3)_2-C_6H_{12}-N^+(CH_3)_2-C_6H_{12}-N^+(CH_3)_2-C_{22}H_{45}(Br^-)_4$ | 22-N ₄ -22 |
| $C_{22}H_{45}-N^+(CH_3)_2-C_6H_{12}-N^+(CH_3)_2-CH_2-(p-C_6H_4)-CH_2-N^+(CH_3)_2-C_6H_{12}-N^+(CH_3)_2-C_{22}H_{45}(Br^-)_2(Cl^-)_2$ | N ₄ -phe |
| $C_{22}H_{45}-N^+(CH_3)_2-C_6H_{12}-N^+(CH_3)_2-CH_2-(p-C_6H_4)-CH_2-N^+(CH_3)_2-C_6H_{12}-N^+(CH_3)_2-CH_2-(p-C_6H_4)-CH_2-N^+(CH_3)_2-C_6H_{12}-N^+(CH_3)_2-C_{22}H_{45}(Br^-)_2(Cl^-)_4$ | N ₆ -diphe |
| $C_{22}H_{45}-N^+(CH_3)_2-C_6H_{12}-N^+(CH_3)_2-CH_2-(p-C_6H_4)-CH_2-N^+(CH_3)_2-C_6H_{12}-N^+(CH_3)_2-CH_2-(p-C_6H_4)-CH_2-N^+(CH_3)_2-C_6H_{12}-N^+(CH_3)_2-CH_2-(p-C_6H_4)-CH_2-N^+(CH_3)_2-C_6H_{12}-N^+(CH_3)_2-C_{22}H_{45}(Br^-)_2(Cl^-)_6$ | N ₈ -triphe |

Table S2. Relative concentration of external acid sites compared to total Al sites.

| Sample | Si/Al ratio | External acid sites/total Al sites |
|---|-------------|------------------------------------|
| Disordered beta (N ₆ -diphe) | 14 | 34 % |
| Bulk beta | 15 | 6 % |
| Hexagonally crystalline MMS | 15 | 44 % |

7. References

1. A. Corma, *Chem. Rev.* **97**, 2373 (1997).
2. U. Ciesla, F. Schüth, *Microporous Mesoporous Mater.* **27**, 131 (1999).
3. M. E. Davis, *Nature* **417**, 813 (2002).
4. C. S. Cundy, P. A. Cox, *Chem. Rev.* **103**, 663 (2003).
5. R. A. Sheldon, R. S. Downing, *Appl. Catal. A-Gen.* **189**, 163 (1999).
6. R. Rinaldi, F. Schüth, *Energy Environ. Sci.* **2**, 610 (2009).
7. J. S. Beck *et al.*, *Chem. Mater.* **6**, 1816 (1994).
8. J. Sun *et al.*, *Nature* **458**, 1154 (2009).
9. C. T. Kresge, M. E. Leonowicz, W. J. Roth, J. C. Vartuli, J. S. Beck, *Nature* **359**, 710 (1992).
10. A. Taguchi, F. Schüth, *Microporous Mesoporous Mater.* **77**, 1 (2005).
11. J. Pérez-Ramirez, C. H. Christensen, K. Egeblad, C. H. Christensen, J. C. Groen, *Chem. Soc. Rev.* **37**, 2530 (2008).
12. A. Karlsson, M. Stöcker, R. Schmidt, *Microporous Mesoporous Mater.* **27**, 181 (1999).
13. Y. Liu, W. Z. Zhang, T. J. Pinnavaia, *J. Am. Chem. Soc.* **122**, 8791 (2000).
14. Z. T. Zhang *et al.*, *J. Am. Chem. Soc.* **123**, 5014 (2001).
15. M. Choi *et al.*, *Nature Mater.* **5**, 718 (2006).
16. K. Egeblad, C. H. Christensen, M. Kustova, C. H. Christensen, *Chem. Mater.* **20**, 946 (2008).
17. W. Fan *et al.*, *Nature Mater.* **7**, 984 (2008).
18. M. Choi *et al.*, *Nature* **461**, 246 (2009).
19. K. Na *et al.*, *J. Am. Chem. Soc.* **132**, 4169 (2010).
20. Materials and methods are available as supporting material on Science Online.
21. R. Ryoo, J. M. Kim, C. H. Ko, C. H. Shin, *J. Phys. Chem.* **100**, 17718 (1996).
22. A. J. Vega, *J. Am. Chem. Soc.* **110**, 1049 (1988).
23. $Q^n(m\text{ Al})$ ^{29}Si species refer to four-coordinate ^{29}Si atoms covalently bonded to four oxygen atoms with n next-nearest-neighbor Si or Al atoms (an integer value between 0 and 4) and m next-nearest-neighbor Al atoms (an integer between 0 and n).
24. M. T. Janicke *et al.*, *J. Am. Chem. Soc.*, **120**, 6940 (1998).
25. E. P. Barrett, L. G. Joyner, P. P. Halenda, *J. Am. Chem. Soc.* **73**, 373 (1951).
26. P. I. Ravikovitch, S. C. Odomhnaill, A. V. Neimark, F. Schuth, K. K. Unger, *Langmuir* **11**, 4765 (1995).
27. A. Saito, H. C. Foley, *Microporous Mater.* **3**, 543 (1995).
28. E. L. Wu, S. L. Lawton, D. H. Olson, A. C. Rohrman Jr., G. T. Kokotailo, *J. Phys. Chem.* **83**, 2777 (1979).
29. R. Ryoo, S. H. Joo, S. Jun, *J. Phys. Chem. B* **103**, 7743 (1999).
30. J. B. Higgins *et al.*, *Zeolites* **8**, 446 (1988).
31. A. Corma *et al.*, *Chem. Mater.* **20**, 3218 (2008).
32. J. H. Lunsford, W. P. Rothwell, W. Shen, *J. Am. Chem. Soc.* **107**, 1540 (1985).
33. Q. Zhao *et al.*, *J. Phys. Chem. B* **106**, 4462 (2002).
34. C. Perego, P. Ingallina, *Catal. Today* **73**, 3 (2002).
35. N. He, S. Bao, Q. Xu, *Appl. Catal. A-Gen.* **169**, 29 (1998).
36. G. Sartori, R. Maggi, *Chem. Rev.* **106**, 1077 (2006).
37. J. Deutsch, H. A. Prescott, D. Müller, E. Kemnitz, H. Lieske, *J. Catal.* **231**, 269 (2005).

38. F. Ocampo, H. S. Yun, M. Maciel Pereira, J. P. Tessonier, B. Louis, *Crystal Growth & Design* **9**, 3721 (2009).

References and Notes

1. A. Corma, From microporous to mesoporous molecular sieve materials and their use in catalysis. *Chem. Rev.* **97**, 2373 (1997). [doi:10.1021/cr960406n](https://doi.org/10.1021/cr960406n) [Medline](#)
2. U. Ciesla, F. Schüth, Ordered mesoporous materials. *Microporous Mesoporous Mater.* **27**, 131 (1999). [doi:10.1016/S1387-1811\(98\)00249-2](https://doi.org/10.1016/S1387-1811(98)00249-2)
3. M. E. Davis, Ordered porous materials for emerging applications. *Nature* **417**, 813 (2002). [doi:10.1038/nature00785](https://doi.org/10.1038/nature00785) [Medline](#)
4. C. S. Cundy, P. A. Cox, The hydrothermal synthesis of zeolites: History and development from the earliest days to the present time. *Chem. Rev.* **103**, 663 (2003). [doi:10.1021/cr020060i](https://doi.org/10.1021/cr020060i) [Medline](#)
5. R. A. Sheldon, R. S. Downing, Heterogeneous catalytic transformations for environmentally friendly production. *Appl. Catal. A Gen.* **189**, 163 (1999). [doi:10.1016/S0926-860X\(99\)00274-4](https://doi.org/10.1016/S0926-860X(99)00274-4)
6. R. Rinaldi, F. Schüth, Energy. Design of solid catalysts for the conversion of biomass. *Energy Environ. Sci.* **2**, 610 (2009).
7. J. S. Beck *et al.*, Molecular or supramolecular templating: Defining the role of surfactant chemistry in the formation of microporous and mesoporous molecular sieves. *Chem. Mater.* **6**, 1816 (1994). [doi:10.1021/cm00046a040](https://doi.org/10.1021/cm00046a040)
8. J. Sun *et al.*, The ITQ-37 mesoporous chiral zeolite. *Nature* **458**, 1154 (2009). [doi:10.1038/nature07957](https://doi.org/10.1038/nature07957) [Medline](#)
9. C. T. Kresge, M. E. Leonowicz, W. J. Roth, J. C. Vartuli, J. S. Beck, Ordered mesoporous molecular sieves synthesized by a liquid-crystal template mechanism. *Nature* **359**, 710 (1992). [doi:10.1038/359710a0](https://doi.org/10.1038/359710a0)
10. A. Taguchi, F. Schüth, Ordered mesoporous materials in catalysis. *Microporous Mesoporous Mater.* **77**, 1 (2005). [doi:10.1016/j.micromeso.2004.06.030](https://doi.org/10.1016/j.micromeso.2004.06.030)
11. J. Pérez-Ramírez, C. H. Christensen, K. Egeblad, C. H. Christensen, J. C. Groen, Hierarchical zeolites: Enhanced utilisation of microporous crystals in catalysis by advances in materials design. *Chem. Soc. Rev.* **37**, 2530 (2008). [doi:10.1039/b809030k](https://doi.org/10.1039/b809030k) [Medline](#)
12. A. Karlsson, M. Stöcker, R. Schmidt, Composites of micro- and mesoporous materials: simultaneous syntheses of MFI/MCM-41 like phases by a mixed template approach. *Microporous Mesoporous Mater.* **27**, 181 (1999). [doi:10.1016/S1387-1811\(98\)00252-2](https://doi.org/10.1016/S1387-1811(98)00252-2)
13. Y. Liu, W. Z. Zhang, T. J. Pinnavaia, Steam-stable aluminosilicate mesostructures assembled from zeolite type Y seeds. *J. Am. Chem. Soc.* **122**, 8791 (2000). [doi:10.1021/ja001615z](https://doi.org/10.1021/ja001615z)
14. Z. T. Zhang *et al.*, Mesoporous aluminosilicates with ordered hexagonal structure, strong acidity, and extraordinary hydrothermal stability at high temperatures. *J. Am. Chem. Soc.* **123**, 5014 (2001). [doi:10.1021/ja004138t](https://doi.org/10.1021/ja004138t) [Medline](#)
15. M. Choi *et al.*, Amphiphilic organosilane-directed synthesis of crystalline zeolite with tunable mesoporosity. *Nat. Mater.* **5**, 718 (2006). [doi:10.1038/nmat1705](https://doi.org/10.1038/nmat1705) [Medline](#)

16. K. Egeblad, C. H. Christensen, M. Kustova, C. H. Christensen, Templating mesoporous zeolites. *Chem. Mater.* **20**, 946 (2008). [doi:10.1021/cm702224p](https://doi.org/10.1021/cm702224p)
17. W. Fan *et al.*, Hierarchical nanofabrication of microporous crystals with ordered mesoporosity. *Nat. Mater.* **7**, 984 (2008). [doi:10.1038/nmat2302](https://doi.org/10.1038/nmat2302) [Medline](#)
18. M. Choi *et al.*, Stable single-unit-cell nanosheets of zeolite MFI as active and long-lived catalysts. *Nature* **461**, 246 (2009). [doi:10.1038/nature08288](https://doi.org/10.1038/nature08288) [Medline](#)
19. K. Na *et al.*, Pillared MFI zeolite nanosheets of a single-unit-cell thickness. *J. Am. Chem. Soc.* **132**, 4169 (2010). [doi:10.1021/ja908382n](https://doi.org/10.1021/ja908382n) [Medline](#)
20. Materials and methods are available as supporting material on *Science Online*.
21. R. Ryoo, J. M. Kim, C. H. Ko, C. H. Shin, Disordered molecular sieve with branched mesoporous channel network. *J. Phys. Chem.* **100**, 17718 (1996). [doi:10.1021/jp9620835](https://doi.org/10.1021/jp9620835)
22. A. J. Vega, Heteronuclear chemical-shift correlations of silanol groups studied by two-dimensional cross-polarization magic angle spinning NMR. *J. Am. Chem. Soc.* **110**, 1049 (1988). [doi:10.1021/ja00212a008](https://doi.org/10.1021/ja00212a008)
23. $Q^n(m\text{ Al})$ ^{29}Si species refer to four-coordinate ^{29}Si atoms covalently bonded to four oxygen atoms with n next-nearest-neighbor Si or Al atoms (an integer value between 0 and 4) and m next-nearest-neighbor Al atoms (an integer between 0 and n).
24. M. T. Janicke *et al.*, Aluminum incorporation and interfacial structures in MCM-41 mesoporous molecular sieves. *J. Am. Chem. Soc.* **120**, 6940 (1998). [doi:10.1021/ja972633s](https://doi.org/10.1021/ja972633s)
25. E. P. Barrett, L. G. Joyner, P. P. Halenda, The determination of pore volume and area distributions in porous substances. I. Computations from nitrogen isotherms. *J. Am. Chem. Soc.* **73**, 373 (1951). [doi:10.1021/ja01145a126](https://doi.org/10.1021/ja01145a126)
26. P. I. Ravikovitch, S. C. O. Domhnaill, A. V. Neimark, F. Schueth, K. K. Unger, Capillary hysteresis in nanopores: Theoretical and experimental studies of nitrogen adsorption on MCM-41. *Langmuir* **11**, 4765 (1995). [doi:10.1021/la00012a030](https://doi.org/10.1021/la00012a030)
27. A. Saito, H. C. Foley, High-resolution nitrogen and argon adsorption on ZSM-5 zeolites: Effects of cation exchange and Si/Al ratio. *Microporous Mater.* **3**, 543 (1995). [doi:10.1016/0927-6513\(94\)00064-3](https://doi.org/10.1016/0927-6513(94)00064-3)
28. E. L. Wu, S. L. Lawton, D. H. Olson, A. C. Rohrman Jr., G. T. Kokotailo, ZSM-5-type materials. Factors affecting crystal symmetry. *J. Phys. Chem.* **83**, 2777 (1979). [doi:10.1021/j100484a019](https://doi.org/10.1021/j100484a019)
29. R. Ryoo, S. H. Joo, S. Jun, Synthesis of highly ordered carbon molecular sieves via template-mediated structural transformation. *J. Phys. Chem. B* **103**, 7743 (1999). [doi:10.1021/jp991673a](https://doi.org/10.1021/jp991673a)
30. J. B. Higgins *et al.*, The framework topology of zeolite beta. *Zeolites* **8**, 446 (1988). [doi:10.1016/S0144-2449\(88\)80219-7](https://doi.org/10.1016/S0144-2449(88)80219-7)
31. A. Corma *et al.*, Synthesis and structure of polymorph B of zeolite beta. *Chem. Mater.* **20**, 3218 (2008). [doi:10.1021/cm8002244](https://doi.org/10.1021/cm8002244)

32. J. H. Lunsford, W. P. Rothwell, W. Shen, Acid sites in zeolite Y: A solid-state NMR and infrared study using trimethylphosphine as a probe molecule. *J. Am. Chem. Soc.* **107**, 1540 (1985). [doi:10.1021/ja00292a015](https://doi.org/10.1021/ja00292a015)
33. Q. Zhao *et al.*, Discernment and quantification of internal and external acid sites on zeolites. *J. Phys. Chem. B* **106**, 4462 (2002). [doi:10.1021/jp015574k](https://doi.org/10.1021/jp015574k)
34. C. Perego, P. Ingallina, Recent advances in the industrial alkylation of aromatics: New catalysts and new processes. *Catal. Today* **73**, 3 (2002). [doi:10.1016/S0920-5861\(01\)00511-9](https://doi.org/10.1016/S0920-5861(01)00511-9)
35. N. He, S. Bao, Q. Xu, Fe-containing mesoporous molecular sieves materials: Very active Friedel-Crafts alkylation catalysts. *Appl. Catal. A Gen.* **169**, 29 (1998). [doi:10.1016/S0926-860X\(97\)00347-5](https://doi.org/10.1016/S0926-860X(97)00347-5)
36. G. Sartori, R. Maggi, Use of solid catalysts in Friedel-Crafts acylation reactions. *Chem. Rev.* **106**, 1077 (2006). [doi:10.1021/cr040695c](https://doi.org/10.1021/cr040695c) [Medline](#)
37. J. Deutsch, H. A. Prescott, D. Müller, E. Kemnitz, H. Lieske, Acylation of naphthalenes and anthracene on sulfated zirconia. *J. Catal.* **231**, 269 (2005). [doi:10.1016/j.jcat.2005.01.024](https://doi.org/10.1016/j.jcat.2005.01.024)
38. F. Ocampo, H. S. Yun, M. Maciel Pereira, J. P. Tessonnier, B. Louis, Design of MFI zeolite-based composites with hierarchical pore structure: A new generation of structured catalysts. *Cryst. Growth Des.* **9**, 3721 (2009). [doi:10.1021/cg900425](https://doi.org/10.1021/cg900425)